APPLICATION OF CHARACTERISTIC BASIS FUNCTION METHOD FOR SCATTERING FROM AND PROPAGATION OVER TERRAIN PROFILES

A THESIS

SUBMITTED TO THE DEPARTMENT OF ELECTRICAL AND

ELECTRONICS ENGINEERING

AND THE INSTITUTE OF ENGINEERING AND SCIENCE

OF BILKENT UNIVERSITY

IN PARTIAL FULFILLMENT OF THE REQUIREMENTS

FOR THE DEGREE OF

MASTER OF SCIENCE

By

Atacan Yağbasan

July, 2009

I certify that I have read this thesis and that in my opinion it is fully adequate, in scope and in quality, as a thesis for the degree of Master of Science.

Assoc. Prof. Dr. Vakur B. Ertürk (Advisor)

I certify that I have read this thesis and that in my opinion it is fully adequate, in scope and in quality, as a thesis for the degree of Master of Science.

Prof. Dr. Ayhan Altıntaş

I certify that I have read this thesis and that in my opinion it is fully adequate, in scope and in quality, as a thesis for the degree of Master of Science.

Assoc. Prof. Dr. Özlem Aydın Çivi

Approved for the Institute of Engineering and Science:

Prof. Dr. Mehmet Baray
Director of the Institute

ABSTRACT

APPLICATION OF CHARACTERISTIC BASIS FUNCTION METHOD FOR SCATTERING FROM AND PROPAGATION OVER TERRAIN PROFILES

Atacan Yağbasan
M.S. in Electrical and Electronics Engineering
Supervisor: Assoc. Prof. Dr. Vakur B. Ertürk
July, 2009

A computationally efficient hybrid method, that combines the characteristic basis function method and the physical optics as well as the forward backward method, is applied for the solution of integral equations used to investigate the electromagnetic scattering from and propagation over large scale rough terrain problems. The method utilizes high-level basis functions defined on macro-domains (named as blocks) namely characteristic basis functions that are constructed by aggregating low-level basis functions (i.e., conventional sub-domain basis functions). In the construction of the abovementioned characteristic basis functions, forward backward method as well as the physical optics approach (when applicable) are used. The conventional characteristic basis function method originally developed by Prakash *et al.* is slightly modified to handle large terrain problems, and is further embellished by accelerating it and by reducing its storage requirements via the use of an extrapolation procedure. Numerical results for the induced currents, total fields and path loss are presented and compared with either measured or previously published reference solutions to assess the efficiency and the accuracy of the method. Besides, certain parametric studies and convergence tests have been carried out.

Keywords: Electromagnetic Scattering, Method of Moments, Forward-Backward Method, Physical Optics, Characteristic Basis Function Method.

ÖZET

KARAKTERİSTİK TEMEL FONKSİYONU METODU İLE ARAZİ KESİTLERİNDE DALGA YAYINIMI VE SAÇILIMI UYGULAMALARI

Atacan Yağbasan
Elektrik ve Elektronik Mühendisliği, Yüksek Lisans
Tez Yöneticisi: Assoc. Prof. Dr. Vakur B. Ertürk
Temmuz, 2009

Geniş ve pürüzlü arazi kesitlerinde elektromanyetik saçılım ve yayınım problemleri için, Karakteristik Temel Fonksiyon Metodu'nu, Fiziksel Optik ve İleri - Geri Yöntemi ile birleştiren etkin bir hibrit metot kullanılmıştır. Metot düşük düzeyli temel fonksiyonların bir araya getirilmesiyle oluşturulan, makro-uzayda (bloklarda) tanımlı karakteristik temel fonksiyonları kullanmaktadır. Yukarıda bahsedilen karakteristik temel fonksiyonlarının oluşturulmasında, ileri-geri yöntemi ve fiziksel optik kullanılmıştır. Prakash tarafından geliştirilen bilindik karakteristik temel fonksiyon metodu, geniş arazi kesit problemlerini çözebilecek şekilde değiştirilmiş, hızlandırılmış ve extrapolasyon tekniği kullanılarak hafıza gereksinimleri azaltılmıştır. Metodun etkinliğini ve doğruluğunu değerlendirmek için, nümerik sonuçlar endüklenen akım, toplam alan ve kayıp cinsinden verilmiş ve daha önce ölçülen ve yayınlanan referans çözümleriyle karşılaştırılmıştır. Ayrıca belli parametrik çalışmalar ve yakınsama testleri yapılmıştır.

Anahtar sözcükler: Elektromanyetik Saçılım, Moment Metodu, İleri-Geri Yöntemi, Fiziksel Optik, Karakteristik Temel Fonksiyonu Metodu.

To My Parents

who sacrificed many of their dreams without expecting any return

and

To My Brother

who has been so much more than a brother

Acknowledgement

I would like to express my deepest gratitude to my advisor Assoc. Prof. Vakur B. Ertürk for his instructive comments and continuing support for the supervision of the thesis. Besides, I am also grateful for his advices that I will keep in mind throughout my life.

I would like to express my special thanks to Prof. Ayhan Altıntaş and Assoc. Prof. Dr. Özlem Aydın Çivi for showing keen interest to the subject matter and accepting to read and review the thesis.

I would also like to thank Prof. Raj Mittra of Pennsylvania State University for his valuable comments and contributions.

I would like to express my sincere appreciation for Dr. Celal Alp Tunç not only for his contributions but also for his friendship. This thesis would never be at this stage without his help.

I would also like to thank Aselsan Inc. for letting me involve in this thesis study and my collegues for their understanding.

Special thanks to TUBITAK for the valuable financial support.

Finally, I would like to thank my parents and my brother for their love, trust and every kind of support throughout my life.

Contents

List of Figures

Chapter 1

Introduction

With the recent advances in wireless technology, accurate computation of electromagnetic wave scattering over large terrain profiles has become of great concern, both for military and commercial applications [1],[2]. With the advent of remote-sensing from airborne platforms using high resolution synthetic aperture techniques, low-grazing angle backscattering turned out to play a crucial role for electronic warfare since backscattered field allowed monitoring of the terrain profile. On the other hand, accurate prediction of electromagnetic field strengths is also important for commercial applications as well, since frequency allocation and cell planning require coverage analysis with varying transmitter and receiver locations.

Even though, analytical models regarding free-space propagation, ground reflection, etc. have been developed, they are only robust in a limited variety of cases since they cannot account for multiple scattering and shadowing, which is the case for low-grazing-angle incidence. For this reason, numerical methods such as integral equation based approaches, which allow direct solution using Maxwell's equations, have become more and more appealing and have been used as a reference solution to validate measurements.

Majority of the integral equation based methods are solved using Method of Moments [3] based solution methods. In all these methods, the main goal is to

minimize the computational cost in terms of central processing unit (CPU) time and storage requirements. A method of moments discretization of an integral equation that describes scattering from a rough surface, yields a system of linear equations that must be solved to obtain the surface current density. Direct solution of the system via lower/upper (LU) decomposition requires order N^3 $[O(N^3)]$ floating point operations, where N is the number of unknowns to be found. This is typically the most expensive step in a MoM analysis of a scattering problem. As the problem geometry becomes larger in terms of wavelength, (i.e., electrical length of the terrain profile increases) the size of the associated MoM matrix grows very rapidly and this, in turn, places an inordinately heavy burden on the CPU in terms of memory and time. Furthermore, a particularly challenging problem occurs when the incident angle approaches the mean horizontal plane containing the rough surface (i.e., low-grazing angles). As the incident angle approaches to horizontal, the region over which the currents are nonzero on the surface increases due to the fact that the projection of the incident beamwidth on the surface increases. As a result, a larger number of surface unknowns (N) must be considered and therefore, more powerful numerical methods become necessary.

The computational expense of direct solution of the system via LU decomposition has lead to the use of iterative solution methods [4]. Non-stationary iterative techniques [5],[6] are extensions of the standard conjugate gradient method, and they are robust in the sense that they are not affected by the order of the surface interactions in the impedance matrix. Hence, they can handle any kind of arbitrarily shaped scattering geometries such as re-entrant surfaces. However, their ability to converge is not as fast as that of stationary algorithms. Without preconditioning techniques, the number of iterations to approach a desired level of error often reaches to hundreds. In order to use a preconditioner, the entries of the impedance matrix should be evaluated and stored, so that the use of non-stationary algorithms are not as computationally efficient as the use of stationary ones.

The Forward-Backward Method (FBM), which is a stationary iterative technique, was developed by Holliday *et al.* [7], [8] for solving the magnetic field integral equation (MFIE), which describes the current induced on a perfectly

conducting (PEC) surface. A similar approach called the method of ordered multiple interactions (MOMI), has been simultaneously proposed by Kapp and Brown [9]. Later on, Holliday *et al.* extended FBM to imperfect conductors in [10]. Both of these approaches are based on splitting the current at each point into two components: the forward contribution due to the incident field and the radiation of the current elements located in front of the receiving element, and the backward contribution due to the current elements located beyond the receiving element. The forward component is first found over the whole surface and then it is used to determine the backward contribution. This is repeated in an iterative process until a converged solution is reached. These methods have been proven to be very accurate and have shown a very fast convergence, giving accurate results within few iterations. However, the operational count per iteration is $O(N^2)$ and this makes the method inefficient when a very large scale terrain profile is regarded.

In order to further reduce the operational count of the iterative methods, the Spectral Acceleration algorithm was proposed by Chou and Johnson in order to analyze quasi-planar (slightly rough), such as ocean-like surfaces [11], [12]. Based on a spectral representation of the two-dimensional Green's function and an appropriate contour deformation, the spectral acceleration algorithm aims to accelerate the matrix-vector multiplications in the FBM by dividing the elements into two groups for a given receiving element: strong interaction and weak interaction groups. The criterion that defines these groups is the distance from the receiving element. Since bigger portion of the elements are grouped as weak interaction, and their contribution is easily computed with the use of the spectral representation of Green's function, the operational count and memory requirements are reduced to $O(N)$ per iteration.

The Spectral Acceleration Forward-Backward Method (SA-FBM) is very efficient when it is applied to slightly rough, such as ocean-like surfaces. Lopez *et al.* modified the integration contour of the method in order to implement SA-FBM to very undulating rough surfaces such as terrain profiles [13]. However, as the roughness of the profile is further increased, the spectral acceleration algorithm

fails to provide accurate results owing to convergence problems during the computation of the weak region contribution. For terrain profiles with large height variations, it may not be possible to define integration paths in the complex plane avoiding sudden exponential growths of the integrand. This makes the method impractical and highly dependent on the geometry.

More recently, Prakash and Mittra proposed the Characteristic Basis Function Method (CFBM) [14]. This approach is based on the characteristic basis functions (CBFs); special functions defined on macro domains (blocks), that include a relatively large number of conventional sub-domains discretized by using pulse functions. Use of these basis functions leads to a significant reduction in the number of unknowns, and results in a substantial size reduction of the MoM matrix. This in turn enables us to handle the reduced matrix by using a direct solver without the need to iterate.

In this thesis, a hybrid approach which combines the characteristic basis function method with the forward-backward method and the physical optics solution (when applicable), has been developed for accurate and efficient solution of electromagnetic scattering and propagation problems that involve large scale and rough terrains. The method is based on the construction of the CBFs with the aid of either PO or FBM. Briefly, the terrain is partitioned into M blocks each of which contains many sub-domain basis functions. Then, primary basis functions (PBFs) and secondary basis functions (SBFs), that constitute the CBFs, are obtained using either PO (when applicable) or FBM, and FBM, respectively. Then, similar to the conventional CBFM, a new matrix equation is formed using the abovementioned CBFs leading to a significantly small-size reduced matrix that can be solved directly. Note that the two important attributes of CBFM are: (i) It rigorously accounts for the mutual interaction effects through the use of SBFs and hence, it preserves the rigors of MoM. (ii) It is iteration free. Thus, CBFM stands as an attractive choice for analyzing electromagnetic scattering problems involving large scale and significantly rough terrain problems.

On the other hand, some modifications/approximations are performed on the conventional CBFM to suit it to terrain problems and hence, to improve both

computational cost and memory storage requirements of the method. First of all, because the mutual interactions between far away elements on a terrain are very weak, only the mutual interactions between the adjacent blocks are retained. However, more neighboring blocks can be included to consider more dominant mutual interactions around the source locations. Morever, during the generation of the reduced matrix, an extrapolation process is used.

The method is applied for radar cross section (RCS) calculations of two-dimensional (2-D) faceted objects [15] as well as three-dimensional (3-D) objects [16], and very accurate results are obtained. The method is also applied for the analysis of microwave circuits [17] and microstrip antennas [18]. In [19], a spectral domain integral equation method is developed that makes the problem be reduced to a matrix equation having dimensions that do not depend on the size of the faceted object but only on its shape. Besides, in order to further improve the efficiency of the method, a sparse representation of the impedance matrix is utilized in [20] and in order to handle multiple excitations efficiently, excitation independent characteristic basis functions approach is proposed in [21]. In addition to these, in [22] Garcia *et al.* further improved the efficiency of the method by combining CBFM with Multilevel Fast Multipole Algorithm (MLFMA). Such a combination avoids the need to calculate and store the coupling terms in the reduced matrix that are not close to the diagonal, thereby optimizing the CPU time and the memory storage requirements. CBFM is first applied for terrain profiles in [23]. The conventional CBFM is slightly modified and hybridized with FBM to handle large terrain profiles. In [24], its computational cost is further reduced in terms of both storage and CPU time via the use of an extrapolation process

The organization of this thesis is as follows: In Chapter 2, background information involving integral equation formulations for both horizontal and vertical polarizations are given. Furthermore, previous approaches such as FBM, GFBM and SA-FBM, that are used in this thesis are also discussed. Chapter 3 is devoted for the formulation of the Characteristic Basis Function Method for large-scale terrain profiles. Numerical results are presented and compared with measured as well as the previously-published reference solutions in Chapter 4 to demonstrate

the accuracy and the numerical efficiency of the method. A discussion on some of the parametric tests that are performed on such terrains is also included. An e^{jwt} time dependence is assumed and suppressed throughout this thesis, where $\omega = 2\pi f$ with f being the operating frequency.

Chapter 2

Background

2.1 Integral Equation Formulation for Impedance Surfaces

For the computation of the scattered fields over a one-dimensional rough surface profile which is illuminated by an electromagnetic source, an integral equation (IE) formulation is carried out where the unknown current density is a part of the integrand. Consequently, a relationship between the incident field and the induced current on the surface is established.

Fig. 2.1 illustrates such a one-dimensional $(1-D)$ rough terrain profile characterized with the surface height profile C defined by $z = f(x)$, along the x-axis, which is embedded in a $2-D$ space ($x-z$ plane). Both the surface height profile and the electromagnetic fields are assumed to be constant along the y-direction. The terrain is considered to be an imperfect conductor, modeled by the surface impedance $\eta_s(\boldsymbol{\rho})$ ($\boldsymbol{\rho} = \hat{x}x + \hat{z}z$) along the surface. Assuming that the scattering surface has a finite conductivity, σ, and the relative permittivity of the scattering surface is large, the impedance boundary condition (IBC), which allows the surface to be treated using a single surface integral equation, can be applied. Detailed information about impedance boundary condition can be found

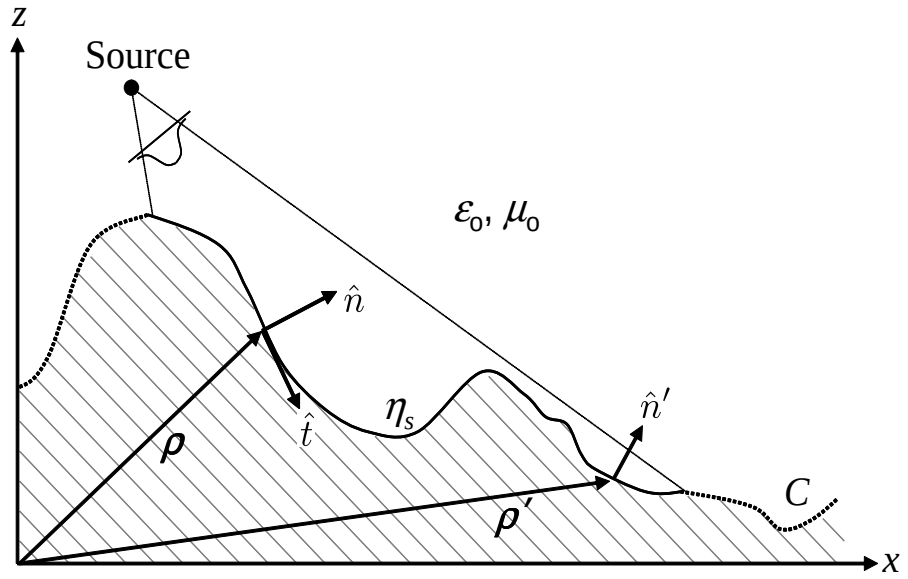

Figure 2.1: Problem Geometry

in [25]-[27].

With the use of surface equivalence theorem [28], an equivalent exterior problem for the rough surface profile illustrated in Fig. 2.1 can be obtained using electric and magnetic sources $\mathbf{J}$ and $\mathbf{M}$, respectively. Equivalent sources on the surface can be defined with the following equations

$$\mathbf{J} = \hat{n} \times \mathbf{H} \tag{2.1}$$

$$\mathbf{M} = \mathbf{E} \times \hat{n} \ . \tag{2.2}$$

Since the relative permittivity is large, the equivalent sources of (2.1) and (2.2) satisfy the IBC with the following equation:

$$\mathbf{M} = \eta_s(\boldsymbol{\rho})\mathbf{J}(\boldsymbol{\rho}) \times \hat{n}(\boldsymbol{\rho}) \tag{2.3}$$

where $\hat{n}$ is the unit normal vector to the surface and η_s is the surface impedance which may vary along the surface. IBC relates the tangential components of the electric surface fields to the magnetic surface fields via a surface impedance η_s defined by the elecromagnetic properties of the scatterer. Since this approximate boundary condition relates only the fields above the surface profile, the scattered fields can be evaluated without the involvement of the fields below; thus,

the analysis of scattering problems is considerably simplified. Note that, IBC approach is limited to media that have complex relative permittivities of 20 in magnitude and greater [29].

The most convenient way of computing the scattered fields for a general wave polarization, is to decompose the field into its parallel and perpendicular components relative to the plane of incidence, and analyze each one of them separately. The total field will be the vector some of these two polarizations.

In general there are various forms of integral equations. Two of the most popular for time-harmonic electromagnetics are the *electric field integral equation* (EFIE) and the *magnetic field integral equation* (MFIE). The EFIE enforces the boundary condition on the tangential electric field and the MFIE enforces the boundary condition on the tangential components of the magnetic field. Both of these equations will be discussed in the following subsections.

2.1.1 EFIE Formulation for Horizontal Polarized Incidence on Non-PEC Surfaces

The transverse magnetic (TM_y) case, in which the electric field is perpendicular to the plane of incidence in Fig. 2.1, is defined as the horizontal polarization case ($\mathbf{E}^{inc} = \hat{y}E^{inc}$). For ($\mathrm{TM}_y$) case, (2.1) and (2.2) state that equivalent sources have normal and tangential components J_y and M_t, respectively. If an impedance boundary condition is valid, (2.3) reduces to

$$E_y(\boldsymbol{\rho}) = \eta_s(\boldsymbol{\rho})J_y(\boldsymbol{\rho}) \tag{2.4}$$

where $E_y(\boldsymbol{\rho})$ denotes the total electric field on the scattering surface. Since $E_y(\boldsymbol{\rho}) = E^{inc}(\boldsymbol{\rho}) + E^{scat}(\boldsymbol{\rho})$, an EFIE is obtained by expressing (2.4) as

$$-E^{inc}(\boldsymbol{\rho}) = -\eta_s(\boldsymbol{\rho})J_y(\boldsymbol{\rho}) + E^{scat}(\boldsymbol{\rho}). \tag{2.5}$$

The TM problem is treated by an E-field formulation in this section and the TE problem will be treated by an H-field formulation in the following section.

Actually, both cases can be treated either by an E-field formulation or an H-field formulation.

The scattered field $\mathbf{E}^{scat}$ can be expressed as the superposition of the individual fields due to $\mathbf{A}$ and $\mathbf{F}$ as follows

$$\mathbf{E}^{scat} = \mathbf{E}_A + \mathbf{E}_F \tag{2.6}$$

where $\mathbf{E}_A$ and $\mathbf{E}_F$ are the fields due to the magnetic and electric vector potentials $\mathbf{A}$ and $\mathbf{F}$, respectively. The following equations hold for the two vector potentials.

$$\mathbf{E}_A = -j\omega\mathbf{A} - j\frac{1}{\omega\mu\epsilon}\nabla(\nabla\cdot\mathbf{A}) \ , \tag{2.7}$$

$$\mathbf{E}_F = -\frac{1}{\epsilon}\nabla\times\mathbf{F} \ . \tag{2.8}$$

In (2.7)-(2.8), ϵ and μ are the permittivity and permeability of the medium above the rough surface, respectively. Since the electric field is horizontally polarized, after performing the curl, divergence and gradient operations, (2.7) and (2.8) can be combined with (2.6) to obtain the equation in the following form.

$$\mathbf{E}^{scat} = \hat{a}_y\left[-j\omega A_y - j\frac{1}{\omega\mu\epsilon}\left(\frac{\partial^2 A_x}{\partial x\partial y} + \frac{\partial^2 A_y}{\partial y^2} + \frac{\partial^2 A_z}{\partial y\partial z}\right) - \frac{1}{\epsilon}\left(\frac{\partial F_x}{\partial z} - \frac{\partial F_z}{\partial x}\right)\right] \ . \tag{2.9}$$

Since there is no y-dependence, the second term in (2.9) vanishes, and EFIE can be written entirely in terms of the equivalent electric current density J_y on the surface as

$$-E_y^{inc}(\boldsymbol{\rho}) = -\eta_s(\boldsymbol{\rho})J_y(\boldsymbol{\rho}) - j\omega A_y - \frac{1}{\epsilon}\left(\frac{\partial F_x}{\partial z} - \frac{\partial F_z}{\partial x}\right) \ . \tag{2.10}$$

The vector potentials $\mathbf{A}$ and $\mathbf{F}$ can be expressed as

$$A_y(\boldsymbol{\rho}) = \mu\int_C J_y(\boldsymbol{\rho}')G(\boldsymbol{\rho},\boldsymbol{\rho}')d\rho' \tag{2.11}$$

$$\mathbf{F}_t(\boldsymbol{\rho}) = \epsilon\int_C \hat{t}(\boldsymbol{\rho}')\eta_s(\boldsymbol{\rho}')J_y(\boldsymbol{\rho}')G(\boldsymbol{\rho},\boldsymbol{\rho}')d\rho' \tag{2.12}$$

where $\hat{t} = \hat{y}\times\hat{n}$ is the unit tangent vector along the surface. $\mathbf{F}_t$ denotes the tangential component of the electric field vector potential and G is the two-dimensional Green's function expressed as

$$G(\boldsymbol{\rho},\boldsymbol{\rho}') = \frac{1}{4j}H_0^{(2)}(kR) \tag{2.13}$$

where $H_0^{(2)}$ is the second-kind Hankel function with order zero and

$$R = \sqrt{[x(\boldsymbol{\rho}) - x(\boldsymbol{\rho'})]^2 + [z(\boldsymbol{\rho}) - z(\boldsymbol{\rho'})]^2}. \tag{2.14}$$

In (2.14), primed coordinates denote the source locations, whereas unprimed coordinates represent the observation points on the surface.

Substituting (2.11) and (2.12) into (2.10), the electric field integral equation can be written as

$$\begin{aligned} -E_y^{inc}(\boldsymbol{\rho}) = -\eta_s(\boldsymbol{\rho}) J_y(\boldsymbol{\rho}) - j\omega\mu \int_C J_y(\boldsymbol{\rho'}) G(\boldsymbol{\rho},\boldsymbol{\rho'}) d\rho' \\ + \int_C \eta_s(\boldsymbol{\rho'}) J_y(\boldsymbol{\rho'}) \frac{\partial}{\partial n'} G(\boldsymbol{\rho},\boldsymbol{\rho'}) d\rho' \end{aligned} \tag{2.15}$$

where $\frac{\partial}{\partial n'} G$ is the derivative of the two-dimensional Green's function with respect to $\hat{n}'$, the normal vector to the surface at the source point $\boldsymbol{\rho'}$.

In order to prevent the introduction of the non-physical edge effects, the surface profile C is arbitrarily extended to infinity in both directions. Moreover, the illuminated rough surface is confined to a finite region so that the integration in (2.15) can be performed.

The Method of Moments Solution

Once a relationship between the induced current and the incident field is constituted, next step is to use a numerical technique to solve (2.15) for the unknown current density J_y. We first expand $J_y(\boldsymbol{\rho'})$ into a finite series of the form with N segments

$$J_y(\boldsymbol{\rho'}) \cong \sum_{n=1}^{N} I_m p_m(\boldsymbol{\rho'}) \tag{2.16}$$

where $p_m(\boldsymbol{\rho'})$ denotes the *basis (expansion)* functions with unknown coefficients I_m for segment m. In order to reduce the computational burden, *pulse* functions are used as the basis functions which are defined to be a constant value over one segment and zero elsewhere, such that

$$p_m(\boldsymbol{\rho'}) = \begin{cases} 1 & \text{, if } \boldsymbol{\rho'} \in \text{segment } m \\ 0 & \text{, otherwise .} \end{cases} \tag{2.17}$$

Once we substitute (2.16) into (2.15) and test the resultant equation at observation points $\boldsymbol{\rho}_n$ on the surface (at the center of each segment n such that $n = 1, 2, 3, ..., N$), we obtain the following equation,

$$-E_y^{inc}(\boldsymbol{\rho}_n) \cong -\eta_s(\boldsymbol{\rho}_n) I_n - j\omega\mu \sum_{m=1}^{N} I_m \int_{\Delta x_m} G(\boldsymbol{\rho}_n, \boldsymbol{\rho}_m) d\rho'$$

$$+ \sum_{m=1}^{N} I_m \int_{\Delta x_m} \eta_s(\boldsymbol{\rho}_m) \frac{\partial}{\partial n_m} G(\boldsymbol{\rho}_n, \boldsymbol{\rho}_m) d\rho' \ . \tag{2.18}$$

Since this equation is valid for each observation point $\boldsymbol{\rho}_n$, an $N \times N$ system of linear equations can be produced by selecting observation points at the center of each one of N segments. The procedure that is followed to convert a continuous integral equation to a discrete matrix equation is a special case of a general approach known as *Method of Moments*. In our case, the basis functions are pulse functions and the weighting functions are impulses. This is also called *point matching (collocation) with pulse basis functions*. The $N \times N$ system can be written in matrix form as

$$-\begin{bmatrix} E_y^{inc}(\boldsymbol{\rho}_1) \\ E_y^{inc}(\boldsymbol{\rho}_2) \\ \vdots \\ E_y^{inc}(\boldsymbol{\rho}_N) \end{bmatrix} = \begin{bmatrix} Z_{11} & Z_{12} & \dots & Z_{1N} \\ Z_{21} & Z_{22} & \dots & Z_{2N} \\ \vdots & \vdots & \dots & \vdots \\ Z_{N1} & Z_{N2} & \dots & Z_{NN} \end{bmatrix} \begin{bmatrix} I_1 \\ I_2 \\ \vdots \\ I_N \end{bmatrix} \tag{2.19}$$

or can be expressed briefly as

$$\mathbf{V} = \bar{\mathbf{Z}}\ \mathbf{I} \ . \tag{2.20}$$

The entries of the $N \times N$ matrix $\bar{\mathbf{Z}}$, in (2.20), characterizes the self and mutual interactions between the segments of the profile. Thus, this matrix is referred to as the *interaction matrix*. This matrix is also called the *moment method impedance matrix* since $\mathbf{V}$ and $\mathbf{I}$ are interpreted as the voltage and the current vectors, respectively. The entries of the impedance matrix in (2.19) are given by

$$Z_{nm} = \int_{\Delta x_m} \left[-j\omega\mu G(\boldsymbol{\rho}_n, \boldsymbol{\rho}_m) + \eta_m \frac{\partial}{\partial n_m} G(\boldsymbol{\rho}_n, \boldsymbol{\rho}_m) \right] d\rho'. \tag{2.21}$$

In (2.21) $\boldsymbol{\rho}_n$ denotes the observation point on the center of the nth segment whereas $\boldsymbol{\rho}_m$ denotes the source point on the center of the mth segment. Discretizing the surface profile with $\frac{\lambda}{10}$ segments, the elements of the impedance matrix may be approximated as

$$Z_{nm} \cong -\frac{\omega\mu}{4}\Delta x_m H_0^{(2)}(k|\boldsymbol{\rho}_n - \boldsymbol{\rho}_m|) - j\frac{k\eta_m}{4}\Delta x_m H_1^{(2)}(k|\boldsymbol{\rho}_n - \boldsymbol{\rho}_m|)\hat{n}_m \cdot \hat{\rho}_{nm} \quad (2.22)$$

where $H_0^{(2)}$ and $H_1^{(2)}$ are the second kind Hankel functions with order zero and one, respectively, and Δx_m is the length of the mth segment. Besides, $\hat{\rho}_{nm}$ denotes the unit vector in the direction from source $\boldsymbol{\rho}_m$ to the receiving element $\boldsymbol{\rho}_n$ and $\hat{n}_m$ represents the unit normal vector of the surface at ρ_m.

Hankel function is singular for $\boldsymbol{\rho}_n = \boldsymbol{\rho}_m$. This corresponds to the diagonal elements of the impedance matrix and the diagonal terms contribute the most to the solution of the system. Hence, these terms must be evaluated accurately. (2.22) cannot be used for their computation. Therefore, using the small argument approximation of the Hankel functions, diagonal entries of the impedance matrix can be obtained as

$$Z_{mm} \cong -\frac{\omega\mu}{4}\Delta x_m \left[1 - j\frac{2}{\pi}\ln\left(\frac{\gamma k \Delta x_m}{4e}\right)\right] - \frac{\eta_m}{2}, \quad (2.23)$$

where γ is the Euler constant 1.781072418 and $e = 2.718281828$.

When the surface profile is PEC, η_m becomes 0, and the expressions for the mutual and self coupling reduce to the following equations:

$$Z_{nm} \cong -\frac{\omega\mu}{4}\Delta x_m H_0^{(2)}(k|\boldsymbol{\rho}_n - \boldsymbol{\rho}_m|) \ , \quad (2.24)$$

$$Z_{mm} \cong -\frac{\omega\mu}{4}\Delta x_m \left[1 - j\frac{2}{\pi}\ln\left(\frac{\gamma k \Delta x_m}{4e}\right)\right] \ . \quad (2.25)$$

Using (2.24) and (2.25), the MoM impedance matrix can be formed and the system in (2.20) can be solved for the unknown surface current for horizontal polarization.

2.1.2 MFIE Formulation for Vertical Polarized Incidence on Non-PEC Surfaces

The transverse electric (TE_y) case, in which the electric field is parallel to the plane of incidence in Fig. 2.1, is defined as the vertical polarization case ($\mathbf{H}^{inc} = \hat{y}H^{inc}$). For ($TE_y$) case, (2.1) and (2.2) state that equivalent sources have normal and tangential components M_y and J_t, respectively. If an impedance boundary condition is valid, (2.3) reduces to

$$H_y(\boldsymbol{\rho}) = -J_t(\boldsymbol{\rho}) \quad . \tag{2.26}$$

Although the MFIE formulation is used for closed surfaces; since the surface is assumed to be arbitrarily extended to infinity, an MFIE can be used to model the vertical polarization problem [30]. Thus, the MFIE

$$-H_y^{inc}(\boldsymbol{\rho}) = J_t(\boldsymbol{\rho}) + H_y^{scat}(\boldsymbol{\rho}) \tag{2.27}$$

is valid on the surface.

Similar to (2.6), the scattered field $\mathbf{H}^{scat}$ can be expressed as the superposition of the individual fields due to $\mathbf{A}$ and $\mathbf{F}$ as follows

$$\mathbf{H}^{scat} = \mathbf{H}_A + \mathbf{H}_F \tag{2.28}$$

where $\mathbf{H}_A$ and $\mathbf{H}_F$ are the fields due to the magnetic and electric vector potentials $\mathbf{A}$ and $\mathbf{F}$, respectively. The following equations hold for the two vector potentials

$$\mathbf{H}_A = \frac{1}{\mu}\nabla \times \mathbf{A}, \tag{2.29}$$

$$\mathbf{H}_F = -j\omega\mathbf{F} - j\frac{1}{\omega\mu\epsilon}\nabla(\nabla \cdot \mathbf{F}). \tag{2.30}$$

Since the H field has only component in the $\hat{y}$-direction, after performing the curl, gradient and divergence operations, (2.29) and (2.30) can be combined with (2.28) to obtain the following equation

$$\mathbf{H}^{scat} = \hat{a}_y \left[-j\omega F_y - j\frac{1}{\omega\mu\epsilon}\left(\frac{\partial^2 F_x}{\partial x \partial y} + \frac{\partial^2 F_y}{\partial y^2} + \frac{\partial^2 F_z}{\partial y \partial z}\right) + \frac{1}{\mu}\left(\frac{\partial A_x}{\partial z} - \frac{\partial A_z}{\partial x}\right)\right]. \tag{2.31}$$

Since there is no y-dependence, the second term in (2.31) vanishes and the MFIE can be written entirely in terms of the tangential induced current density J_t on the surface as

$$-H_y^{inc}(\boldsymbol{\rho}) = J_t(\boldsymbol{\rho}) - j\omega F_y - \frac{1}{\mu}\left(\frac{\partial A_z}{\partial x} - \frac{\partial A_x}{\partial z}\right). \tag{2.32}$$

The vector potentials $\mathbf{A}$ and $\mathbf{F}$ can be expressed as

$$\mathbf{A}_t(\boldsymbol{\rho}) = \mu \int_C \hat{t}(\boldsymbol{\rho}')J_t(\boldsymbol{\rho}')G(\boldsymbol{\rho},\boldsymbol{\rho}')d\rho' \tag{2.33}$$

$$F_y(\boldsymbol{\rho}) = -\epsilon \int_C \eta_s(\boldsymbol{\rho}')J_t(\boldsymbol{\rho}')G(\boldsymbol{\rho},\boldsymbol{\rho}')d\rho' \tag{2.34}$$

and $\hat{t}$ is the unit tangent vector along the surface.

Substituting (2.33) and (2.34) into (2.32), the final form of the magnetic field integral equation can be obtained as

$$\begin{aligned} -H_y^{inc}(\boldsymbol{\rho}) = J_t(\boldsymbol{\rho}) &+ j\omega\epsilon \int_C \eta_s(\boldsymbol{\rho}')J_t(\boldsymbol{\rho}')G(\boldsymbol{\rho},\boldsymbol{\rho}')d\rho' \\ &- \int_C J_t(\boldsymbol{\rho}')\frac{\partial}{\partial n'}G(\boldsymbol{\rho},\boldsymbol{\rho}')d\rho'. \end{aligned} \tag{2.35}$$

Next step is to apply the discretization process for MFIE as applied in the EFIE to approximate the equivalent current density.

The Method of Moments Solution

Once a relationship between the induced current and the incident field is constituted, next step is to use a numerical technique to solve (2.35) for the unknown current density J_t. We first expand $J_t(\boldsymbol{\rho}')$ into a finite series of the form with N segments

$$J_t(\boldsymbol{\rho}') \cong \sum_{n=1}^{N} I_m p_m(\boldsymbol{\rho}') \ . \tag{2.36}$$

In order to reduce the computational burden, *pulse* functions are used as the basis functions which are defined to be a constant value over one segment and zero elsewhere, such that

$$p_m(\boldsymbol{\rho}') = \begin{cases} 1 & \text{, if } \boldsymbol{\rho}' \in \text{segment } m \\ 0 & \text{, otherwise .} \end{cases} \tag{2.37}$$

Once we substitute (2.36) into (2.35) and test the resultant equation at observation points $\boldsymbol{\rho}_n$ on the surface (at the center of each segment n such that $n = 1, 2, 3, ..., N$), we obtain the following equation

$$-H_y^{inc}(\boldsymbol{\rho}_n) \cong I_n + j\omega\epsilon \sum_{m=1}^{N} I_m \int_{\Delta x_m} \eta_s(\boldsymbol{\rho}_m) G(\boldsymbol{\rho}_n, \boldsymbol{\rho}_m) d\rho'$$

$$- \sum_{m=1}^{N} I_m \int_{\Delta x_m} \frac{\partial}{\partial n_m} G(\boldsymbol{\rho}_n, \boldsymbol{\rho}_m) d\rho'. \tag{2.38}$$

Since this equation is valid for each observation point $\boldsymbol{\rho}_n$, $N \times N$ system of linear equations can be produced by selecting observation points at the center of each one of N segments. The $N \times N$ system can be written in matrix form as

$$-\begin{bmatrix} H_y^{inc}(\boldsymbol{\rho}_1) \\ H_y^{inc}(\boldsymbol{\rho}_2) \\ \vdots \\ H_y^{inc}(\boldsymbol{\rho}_N) \end{bmatrix} = \begin{bmatrix} Z_{11} & Z_{12} & \dots & Z_{1N} \\ Z_{21} & Z_{22} & \dots & Z_{2N} \\ \vdots & \vdots & \dots & \vdots \\ Z_{N1} & Z_{N2} & \dots & Z_{NN} \end{bmatrix} \begin{bmatrix} I_1 \\ I_2 \\ \vdots \\ I_N \end{bmatrix} \tag{2.39}$$

or can be expressed briefly as

$$\mathbf{V} = \bar{\mathbf{Z}}\ \mathbf{I}\ . \tag{2.40}$$

The entries of the impedance matrix in (2.39) are given by

$$Z_{nm} = \int_{\Delta x_m} \left[j\omega\epsilon\eta_m G(\boldsymbol{\rho}_n, \boldsymbol{\rho}_m) - \frac{\partial}{\partial n_m} G(\boldsymbol{\rho}_n, \boldsymbol{\rho}_m) \right] d\rho'. \tag{2.41}$$

Here $\boldsymbol{\rho}_n$ denotes the observation point on the center of the nth segment whereas $\boldsymbol{\rho}_m$ denotes the source point on the center of the mth segment. Discretizing the surface profile with $\frac{\lambda}{10}$ segments, the elements of the impedance matrix may be approximated as

$$Z_{nm} \cong -\frac{\omega\epsilon\eta_m}{4} \Delta x_m H_0^{(2)}(k|\boldsymbol{\rho}_n - \boldsymbol{\rho}_m|) + j\frac{k}{4} \Delta x_m H_1^{(2)}(k|\boldsymbol{\rho}_n - \boldsymbol{\rho}_m|) \hat{n}_m \cdot \hat{\rho}_{nm} \tag{2.42}$$

where $H_0^{(2)}$ and $H_1^{(2)}$ are the second kind Hankel functions with order zero and one, respectively, and Δx_m is the length of the mth segment. Besides, $\hat{\rho}_{nm}$ denotes the unit vector in the direction from source $\boldsymbol{\rho}_m$ to the receiving element ρ_n and $\hat{n}_m$ represents the unit normal vector of the surface at ρ_m.

Hankel function is singular for $\boldsymbol{\rho}_n = \boldsymbol{\rho}_m$. This corresponds to the diagonal elements of the impedance matrix and the diagonal terms contribute the most to the solution of the system. Hence, these terms must be evaluated accurately. (2.42) cannot be used for their computation. Therefore, using the small argument approximation of the Hankel functions, diagonal entries of the impedance matrix can be obtained as

$$Z_{mm} \cong \frac{1}{2} + \frac{\omega\epsilon\eta_m}{4}\Delta x_m \left[1 - j\frac{2}{\pi}\ln\left(\frac{\gamma k \Delta x_m}{4e}\right)\right] \tag{2.43}$$

where γ is the Euler constant 1.781072418 and $e = 2.718281828$.

When the surface profile is PEC, η_m becomes 0, and the expressions for the mutual and self coupling reduce to the following equations by equating η_m to 0:

$$Z_{nm} \cong -j\frac{k}{4}\Delta x_m H_1^{(2)}(k|\boldsymbol{\rho}_n - \boldsymbol{\rho}_m|)\hat{n}_m \cdot \hat{\rho}_{nm} \ , \tag{2.44}$$

$$Z_{mm} \cong \frac{1}{2} \ . \tag{2.45}$$

Following the procedure described above, the moment method impedance matrix, $\bar{\mathbf{Z}}$ with N^2 entries, is generated. In order to solve the system for $\mathbf{I}$ given in (2.40), $\bar{\mathbf{Z}}$ should be inverted. Its direct inversion via Gaussian elimination or LU decomposition has an operational cost with $O(N^3)$. On the other hand, the storage of the matrix has a memory requirement of $O(N^2)$. As the length of the profile increases in terms of wavelength, the size of the associated MoM matrix grows very rapidly and this, in turn, places an inordinately heavy burden on the CPU in terms of memory and time. Therefore, in order to circumvent these problems to a certain point, iterative techniques such as Forward-Backward Method (FBM), which reduces the operational cost to $O(N^2)$ and eliminates the need to store the impedance matrix, has been devised. In the next section, the formulation of FBM is discussed.

2.2 The Formulation of the Forward-Backward Method

Direct solution of the matrix equation $\mathbf{V} = \bar{\mathbf{Z}}\ \mathbf{I}$ via Gaussian elimination or LU decomposition has an operational cost of $O(N^3)$, where N is the number of unknowns in the discretized representation of the surface current.

As the size of the computation domain increases, the computational expense of these operations becomes prohibitive. Besides the $O(N^3)$ operational cost, storage of the impedance matrix with N^2 elements is also a huge burden. This has led to the development of iterative schemes that solve for the surface current in $O(N^2)$ steps.

The FBM is a stationary iterative technique that proposes a *forward* and *backward* decomposition over the matrices and vectors involved in (2.20). FBM starts with the following two decompositions such that

$$\mathbf{I} = \mathbf{I}^f + \mathbf{I}^b \tag{2.46}$$

$$\bar{\mathbf{Z}} = \bar{\mathbf{Z}}^f + \bar{\mathbf{Z}}^s + \bar{\mathbf{Z}}^b \tag{2.47}$$

where $\mathbf{I}^f$ is the forward component denoting the current distribution due to the wave propagation in the forward direction and $\mathbf{I}^b$ is the backward component representing the current distribution due to the wave propagation in the backward direction. On the other hand, $\bar{\mathbf{Z}}^f$, $\bar{\mathbf{Z}}^s$ and $\bar{\mathbf{Z}}^b$ are, respectively, the lower triangular part (forward impedance terms), the diagonal part (self impedance terms) and the upper triangular part (backward impedance terms) of $\bar{\mathbf{Z}}$.

Using (2.46) and (2.47), the original system can be split into forward-propagation and backward-propagation matrix equations, as follows

$$\bar{\mathbf{Z}}^s \cdot \mathbf{I}^f = \mathbf{V} - \bar{\mathbf{Z}}^f \cdot (\mathbf{I}^f + \mathbf{I}^b) \tag{2.48}$$

$$\bar{\mathbf{Z}}^s \cdot \mathbf{I}^b = -\bar{\mathbf{Z}}^b \cdot (\mathbf{I}^f + \mathbf{I}^b)\ . \tag{2.49}$$

The second term in the right-hand side of (2.48) corresponds to the radiation of current elements in front of the nth receiving element in Fig. 2.2, whereas

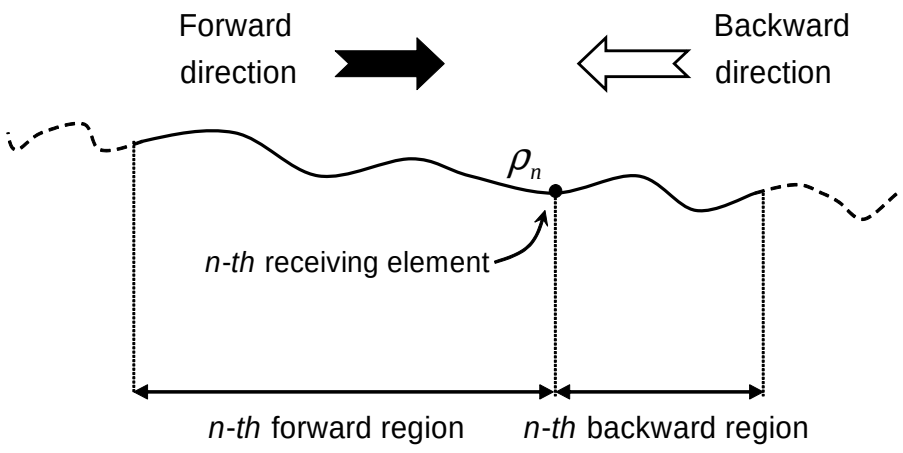

Figure 2.2: Forward and backward regions for the nth matching point

the term on the right-hand side of (2.49) corresponds to the radiation of current elements in the rear of the nth receiving element.

An iterative procedure can be used to solve forward and backward propagation equations by initializing $\mathbf{I}^{b,0} = 0$, and at the qth sweep,

$$(\bar{\mathbf{Z}}^s + \bar{\mathbf{Z}}^f) \cdot \mathbf{I}^{f,(q)} = \mathbf{V} - \bar{\mathbf{Z}}^f \cdot \mathbf{I}^{b,(q-1)} \tag{2.50}$$

$$(\bar{\mathbf{Z}}^s + \bar{\mathbf{Z}}^b) \cdot \mathbf{I}^{b,(q)} = -\bar{\mathbf{Z}}^b \cdot \mathbf{I}^{f,(q)}. \tag{2.51}$$

Since $\bar{\mathbf{Z}}^{\mathbf{s}} + \bar{\mathbf{Z}}^{\mathbf{b}}$ is an upper triangular matrix and $\bar{\mathbf{Z}}^{\mathbf{s}} + \bar{\mathbf{Z}}^{\mathbf{f}}$ is a lower triangular matrix, the matrices in this iterative process do not need to be factorized or inverted. Iterations are continued until surface currents show convergence to within a specified accuracy criterion. The forward contribution in (2.50) can be more explicitly expressed as

$$I_1^{f,(i)} = \frac{V_1^{(i)}}{Z_{1,1}}$$

$$I_n^{f,(i)} = \frac{V_n^{(i)} - (\sum_{k=1}^{n-1} Z_{n,k} I_k^{(i)})}{Z_{n,n}}, \quad \text{with } n = 2, 3, .., N. \tag{2.52}$$

Similarly, the backward contribution in (2.51), can be expressed as

$$I_N^{b,(i)} = 0$$

$$I_n^{b,(i)} = \frac{-(\sum_{k=n+1}^{N} Z_{n,k} I_k^{(i)})}{Z_{n,n}}, \quad \text{with } n = N-1, N-2, .., 1. \tag{2.53}$$

Using FBM, there is no need to store the elements of the impedance matrix because of the sweeping procedure. However, the surface height data, incident field values at matching points, and forward, backward and total currents have to be stored in N element arrays, where N is the surface unknowns. Therefore the memory requirement of the method is $O(N)$. The mutual impedance values are recomputed at each iteration with a computational cost of $O(QN^2)$, where Q is the number of iterations. Since the method obtains very accurate results in a few iterations (usually Q is less than 10), the total computational requirement of the method becomes $O(N^2)$ for large N. On the other hand, since it is mathematically equivalent to the well-known *symmetric successive over relaxation - SSOR* iteration, it can handle problems ending up with diagonally dominant system matrices. Changing the order of current elements disturbs the diagonally dominant nature, which then strongly affects the convergence of the method. The algorithm may become unstable for re-entrant surfaces where current elements are not numbered sequentially as a function of increasing x coordinate.

On the other hand FBM as being a stationary iterative technique provides a more rapid convergence than a standard non-stationary iterative algorithm in many cases. It has been experimented that for TM polarization induced current values converge to an error level about 10^{-3} after six or seven iterations [30]. For TE polarization, since the system matrix is more diagonally dominant, it takes less iterations (typically two or three) to converge to the same level of error. That is why FBM can be used as a numerically accurate reference solution instead of MoM when the length of the surface profile is electrically large, where MoM becomes hard to be applied. However, since the computational requirement of FBM is $O(N^2)$, it is still computationally expensive and becomes difficult to handle when the number of surface unknowns increases. This limitation has been overcome by the Spectral Acceleration Forward Backward Method (SA-FBM), which will be explained briefly in Section 2.4.

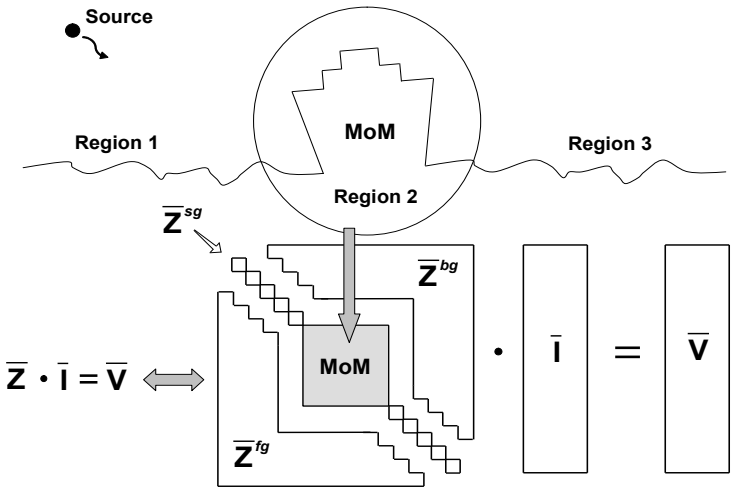

Figure 2.3: Composite problem and matrix decomposition in GFBM

2.3 The Generalized Forward-Backward Method

Consider the composite problem depicted in Fig. 2.3, where one or more PEC obstacles (in Fig. 2.3, the PEC obstacle is a ship) are included in the surface profile. For this kind of problem, conventional FBM does not exhibit convergent behaviour because the presence of the obstacle highly disturbs the propagation process. There are strong interactions between the obstacle and the nearby ocean-like surface, and within the obstacle itself, all of which may not be taken into account with the conventional formulation involved in the standard FB method.

In order to overcome this drawback, the Generalized Forward-Backward Method (GFBM) is proposed in [31], which is a hybrid method based on a combination of the conventional FBM with MoM. GFBM is based on the same general concepts previously stated for FBM, but includes some significant differences mainly in the decomposition of the matrix $\bar{\mathbf{Z}}$ that will be detailed next.

Starting with (2.20), in the same way as done in FBM, the current is expressed as the sum of two contributions

$$\mathbf{I} = \mathbf{I}^f + \mathbf{I}^b \ . \tag{2.54}$$

However, the impedance matrix is split in a different way in GFBM such that

$$\bar{\mathbf{Z}} = \bar{\mathbf{Z}}^{fg} + \bar{\mathbf{Z}}^{sg} + \bar{\mathbf{Z}}^{bg} \tag{2.55}$$

where the $\bar{\mathbf{Z}}^{sg}$ matrix is the diagonal part of $\bar{\mathbf{Z}}$ with an additional block including the impedance submatrix corresponding to the PEC obstacle and nearby ship region; while $\bar{\mathbf{Z}}^{fg}$ and $\bar{\mathbf{Z}}^{bg}$ are, respectively, the lower triangular part and upper triangular part of $\bar{\mathbf{Z}}$ but excluding the matrix $\bar{\mathbf{Z}}^{sg}$, as illustrated in Fig. 2.3. Then, the original system is transformed in a similar way as in the conventional FBM, yielding the following matrix equations:

$$\bar{\mathbf{Z}}^{sg} \cdot \mathbf{I}^{f} = \mathbf{V} - \bar{\mathbf{Z}}^{fg} \cdot (\mathbf{I}^{f} + \mathbf{I}^{b}) \tag{2.56}$$

$$\bar{\mathbf{Z}}^{sg} \cdot \mathbf{I}^{b} = -\bar{\mathbf{Z}}^{bg} \cdot (\mathbf{I}^{f} + \mathbf{I}^{b}) \tag{2.57}$$

which can be iteratively solved for $\mathbf{I}^{f,(q)}$ and $\mathbf{I}^{b,(q)}$ as

$$(\bar{\mathbf{Z}}^{sg} + \bar{\mathbf{Z}}^{fg}) \cdot \mathbf{I}^{f,(q)} = \mathbf{V} - \bar{\mathbf{Z}}^{fg} \cdot \mathbf{I}^{b,(q-1)} \tag{2.58}$$

$$(\bar{\mathbf{Z}}^{sg} + \bar{\mathbf{Z}}^{bg}) \cdot \mathbf{I}^{b,(q)} = -\bar{\mathbf{Z}}^{bg} \cdot \mathbf{I}^{f,(q)} \tag{2.59}$$

starting with $\mathbf{I}^{b,(0)} = 0$.

GFBM is very efficient when it is applied to re-entrant type surface profiles provided that region 2 in Fig. 2.3 involves small portion of the surface unknowns. Since self-interaction matrix of region 2 is stored and directly inverted, computational efficiency of the method is highly dependent on the number of unknowns in this region. On the other hand, regardless of the surface unknowns in region 2, GFBM procedure has still $O(N^2)$ computational cost and is not efficient when applied to electrically large geometries. Spectral acceleration algorithm is adopted to GFBM in [32] to reduce the operational count to $O(N)$. However, direct inversion of the self-interaction matrix for region 2 is still an issue.

2.4 Spectral Acceleration of the FBM over Terrain Profiles

In [11] and [12], Spectral Acceleration (SA) algorithm was developed to reduce the computational cost of FBM to $O(N)$ over one-dimensional slightly rough

PEC surfaces and impedance rough surfaces, respectively. It should be noted that these original implementations of the spectral acceleration algorithm were developed to analyze quasi-planar (slightly rough) surfaces such as ocean-like surfaces, and are not suitable for very undulating geometries. López *et al.* modified the spectral acceleration algorithm in order to implement SA-FBM to very undulating rough surfaces such as terrain profiles [13]. Besides, SA-FBM is utilized for the investigation of existent propagation models in [33].

SA-FBM is based on the fast computation of the radiation of the far elements by using a spectral representation of the 2D Green's function. Thus, the radiating elements over a given receiving element are divided into two groups: *strong interaction group* G_s and *weak interaction group* G_w. The criterion that defines these groups is the distance from the radiating to the receiving element. So for a given distance L_s, the strong group G_s includes the N_s nearest elements to the receiving element while the rest of the radiating elements are included in the weak group G_w as illustrated in Fig. 2.4. With this decomposition, the fields radiated over the receiving element can be expressed as the sum of the weak and strong group contributions.

To start with, SA-FBM formulation for the integral equations derived in Section 2.1 will be described for both horizontal and vertical polarizations. For simplicity only the application of the SA to the forward propagation equation will be described. The same procedure can be applied to model the backward propagation effects.

2.4.1 Horizontal Polarization

Starting with the formulation of the EFIE described in Section 2.1 for the horizontal polarization, the radiated electric field at $\boldsymbol{\rho}_n$ due to the forward propagation E_f and backward propagation E_b can be obtained as:

$$E_f(\boldsymbol{\rho}_n) = \sum_{m=1}^{n-1} I_m Z_{nm} \tag{2.60}$$

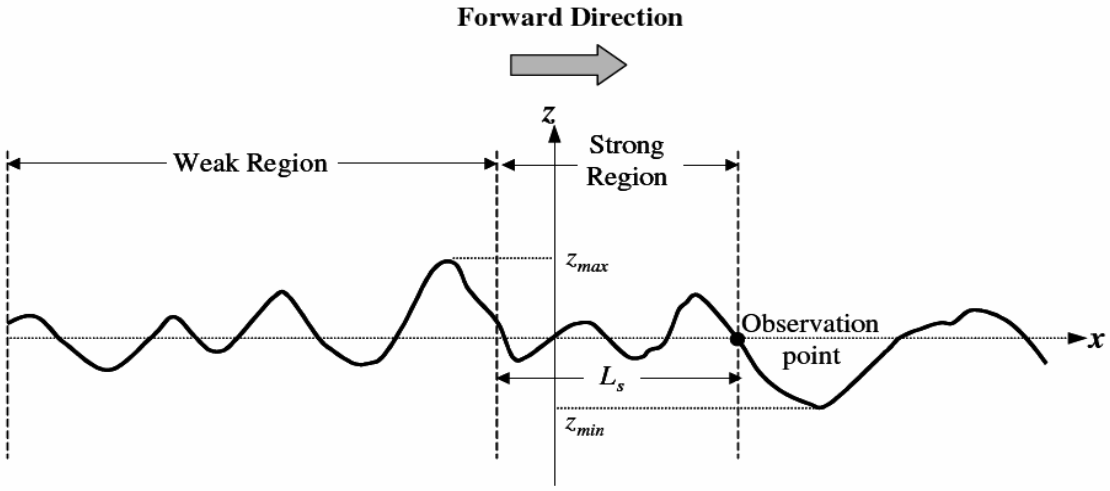

Figure 2.4: 1-D finite rough surface profile

$$E_b(\boldsymbol{\rho}_n) = \sum_{m=n+1}^{N} I_m Z_{nm}. \tag{2.61}$$

E_f is decomposed into the fields radiated by the strong and weak groups, E_s and E_w respectively,

$$\begin{aligned} E_f(\boldsymbol{\rho}_n) &= E_s(\boldsymbol{\rho}_n) + E_w(\boldsymbol{\rho}_n) \\ &= \sum_{m=n-N_s}^{n-1} I_m Z_{nm} + \sum_{m=1}^{n-N_s-1} I_m Z_{nm} \end{aligned} \tag{2.62}$$

where $N_s = L_s/\Delta x$ denotes the number of elements that have strong interactions with the nth element. The off-diagonal entries of the impedance matrix for the horizontal polarization were derived using the EFIE in Section 2.1 for non-PEC surfaces as

$$Z_{nm} = -j\omega\mu G(\boldsymbol{\rho}_n, \boldsymbol{\rho}_m)\Delta x_m + \eta_m \Delta x_m \frac{\partial}{\partial n_m} G(\boldsymbol{\rho}_n, \boldsymbol{\rho}_m). \tag{2.63}$$

The radiation of the strong interaction group is computed directly through a matrix-vector product, but the weak group contribution is obtained by employing the spectral representation of the Green's function and its derivative. The spectral representation of the Green's functions can be expressed as

$$G(\boldsymbol{\rho}_n, \boldsymbol{\rho}_m) = -\frac{j}{4\pi} \int_{C_\phi} e^{-jk[(x_n - x_m)\cos\phi + (z_n - z_m)\sin\phi]} d\phi \tag{2.64}$$

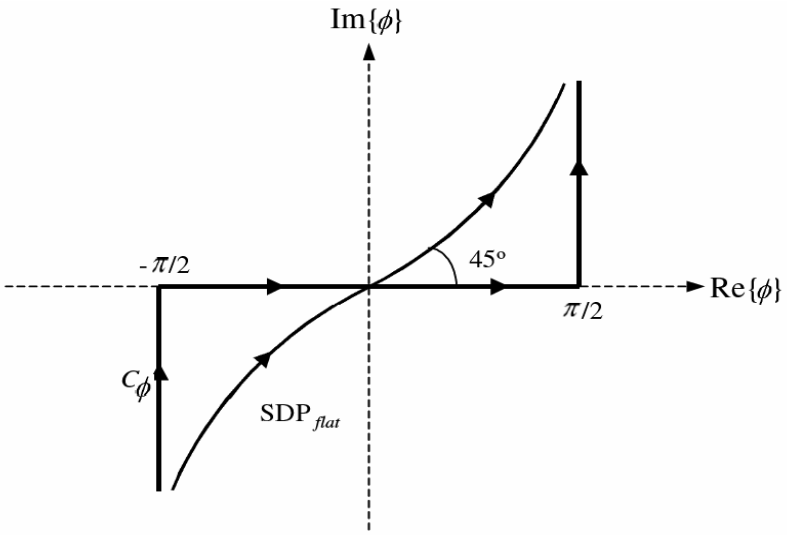

Figure 2.5: Integration path in complex space

where C_ϕ is the contour of integration in the complex ϕ-space (shown in Fig. 2.5). On the other hand, the spectral representation of the partial derivative of the Green's function with respect to the normal vector on the source point can be expressed as:

$$\frac{\partial}{\partial n_m} G(\boldsymbol{\rho}_n, \boldsymbol{\rho}_m) = \frac{k}{4\pi} \int_{C_\phi} [\cos\theta_m \cos\phi + \sin\theta_m \sin\phi] e^{-jk[(x_n - x_m)\cos\phi + (z_n - z_m)\sin\phi} d\phi \tag{2.65}$$

where θ_m is the angle between the unit normal vector to the surface at the source point, $\hat{n}_m$, and the unit vector in the x direction, $\hat{x}$. Introducing (2.64) and (2.65) into the expression for $E_w(\boldsymbol{\rho}_n)$ and interchanging the integration and summation yields to:

$$E_w(\boldsymbol{\rho}_n) = -\frac{\omega\mu}{4\pi} \int_{C_\phi} F_n(\phi) d\phi \tag{2.66}$$

where

$$F_n(\phi) = \sum_{m \in G_w} I_m \Delta x_m \left(1 - \frac{\eta_m}{\eta_0}[\cos\theta_m \cos\phi + \sin\theta_m \sin\phi]\right) \cdot e^{-jk[(x_n - x_m)\cos\phi - (z_n - z_m)\sin\phi]}. \tag{2.67}$$

$F_n(\phi)$ can be obtained from $F_{n-1}(\phi)$ as:

$$F_n(\phi) = F_{n-1}(\phi) e^{-jk[(x_n - x_{n-1})\cos\phi - (z_n - z_{n-1})\sin\phi]}$$

$$+I_{ns}\Delta x_{ns}\left(1-\frac{\eta_{ns}}{\eta_0}[\cos\theta_{ns}\cos\phi+\sin\theta_{ns}\sin\phi]\right)$$
$$\cdot e^{-jk[(x_n-x_{ns})\cos\phi-(z_n-z_{ns})\sin\phi]} \tag{2.68}$$

with $F_n(\phi)=0$ for $n\leq N_s+1$ during the forward sweep, and $n_s=n-N_s-1$ is the new source point introduced in the weak group as the iterative procedure sweeps the surface in the forward direction. An analogous procedure can be followed for backward propagation and is given in Appendix A.

2.4.2 Vertical Polarization

In a similar way, when using the MFIE formulation in the vertical polarization case, the radiating elements are also divided into 2 groups (G_s and G_w) and their contribution to the forward magnetic field H_f can be expressed as follows

$$H_f(\boldsymbol{\rho}_n)=H_s(\boldsymbol{\rho}_n)+H_w(\boldsymbol{\rho}_n)$$
$$=\sum_{m=n-N_s}^{n-1}I_mZ_{nm}+\sum_{m=1}^{n-N_s-1}I_mZ_{nm} \tag{2.69}$$

where H_w and H_s are the fields radiated by the weak and strong groups, respectively, and Z_{nm} is defined in Section 2.1 as

$$Z_{nm}=j\omega\epsilon\eta_m\Delta x_m G(\boldsymbol{\rho}_n,\boldsymbol{\rho}_m)-\Delta x_m\frac{\partial}{\partial n_m}G(\boldsymbol{\rho}_n,\boldsymbol{\rho}_m). \tag{2.70}$$

Using the spectral representation of Green's function and its derivative, contribution due to the weak group can be expressed as:

$$H_w(\boldsymbol{\rho}_n)=-\frac{k}{4\pi}\int_{C_\phi}F_n(\phi)d\phi \tag{2.71}$$

where

$$F_n(\phi)=\sum_{m\in G_w}I_m\Delta x_m\left(\cos\theta_m\cos\phi+\sin\theta_m\sin\phi-\frac{\eta_m}{\eta_0}\right)$$
$$\cdot e^{-jk[(x_n-x_m)\cos\phi-(z_n-z_m)\sin\phi]}. \tag{2.72}$$

Then, $F_n(\phi)$ can be obtained from $F_{n-1}(\phi)$ like in (2.68) except the term inside the paranthesis is changed with $\left(\cos\theta_{ns}\cos\phi+\sin\theta_{ns}\sin\phi-\frac{\eta_{ns}}{\eta_0}\right)$. An analogous procedure can be followed for backward propagation and is given in Appendix A.

Once the integrands F_n have been determined, it is necessary to describe the parameters which define the numerical integration in the complex space. In the following subsections, integration path and the numerical sampling density are described.

2.4.3 Integration Path

Hankel function is analytic in the complex plane for widely separated points, so the integration contour C_ϕ in Fig. 2.5, can be deformed to any other integration path as given in Fig. 2.6. This path is chosen to reduce the computational cost needed to evaluate the integral and to avoid possible exponential growths of the integrand values which would cause numerical errors due to the limited precision of the computer.

As it can be seen in Fig. 2.6, the path is composed by several stretches. The main one is the central stretch denoted by C; if needed two lateral stretches can be added, the left one denoted as L, and the right one will be named as R. All the parameters needed to determine the integration path (the angle δ that the stretch C forms with the real axis and the position of ϕ_1, ϕ_2, ϕ_3 and ϕ_4 points on the complex space) will be defined next. To obtain these parameters, some generic considerations must be taken into account. All these considerations are related to the saddle point distribution in the complex ϕ-space. For a general terrain profile, as the one depicted in Fig. 2.1, saddle points are distributed along the real axis of the complex ϕ plane. Each set of source (placed at $\boldsymbol{\rho}_m$), and receiving element (placed at $\boldsymbol{\rho}_n$) corresponds to a saddle point located at ϕ_{nm}:

$$\phi_{nm} = \tan^{-1}\left(\frac{z_n - z_m}{x_n - x_m}\right) \tag{2.73}$$

such that ϕ_{nm} is limited by the minimum and maximum slopes of the terrain, i.e. $\phi_{nm} \in [\phi_{s,min}, \phi_{s,max}]$. It is important to notice that for an irregular terrain, the saddle points are not distributed in a homogeneous manner along the real axis. For a downhill profile, saddle points will be placed at $\phi_{nm} < 0$, but for an uphill geometry they will be placed at $\phi_{nm} > 0$. For a generic terrain, a medium angle ϕ_{med} can be obtained from the mean value of all saddle point values. This

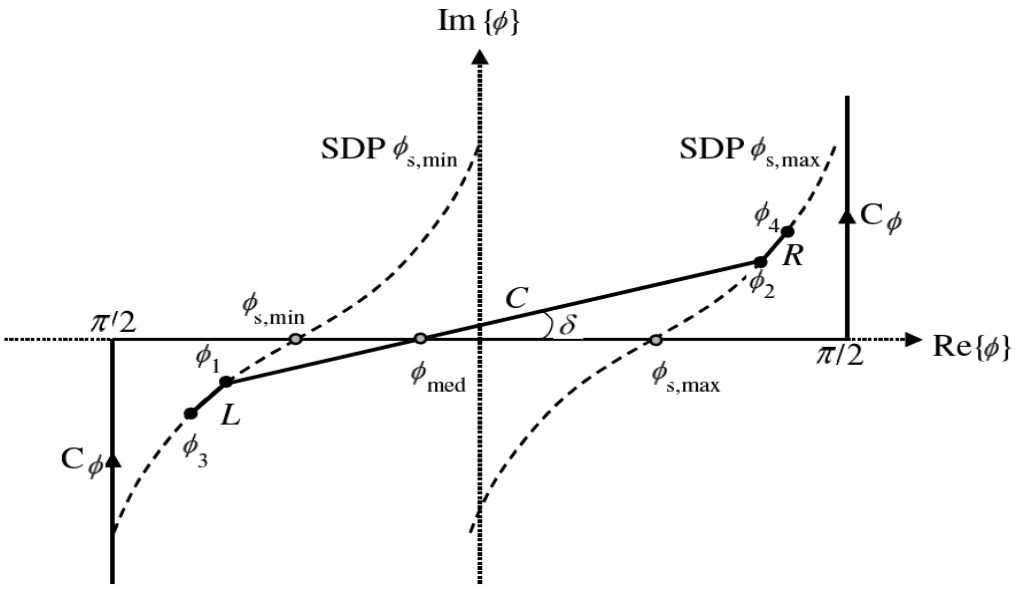

Figure 2.6: Deformed integration path in the complex space

angle ϕ_{med} gives a general idea of the terrain slope and the position of the saddle points. It is desirable to center the integration path with respect to the saddle point distribution, so the central stretch C will be centered at ϕ_{med} (cross-point of this stretch with real axis), as shown in Fig. 2.6.

To completely determine the stretch C, the angle δ formed with the real axis must be defined. The inclination angle of the central path δ is determined by limiting the contribution due to the most critical saddle point over the deformed contour. The limit proposed in [11] is not valid because it was obtained considering the special geometric characteristics of ocean-like rough surfaces. When the geometries under study present important height variations, this limit must be redefined. Through empirical tests it has been found that a value of e^2 is a nearly optimum choice to limit this contribution, even though smaller values can be used. Upon this consideration, the angle δ must follow the expression:

$$\tan\delta = \min\left[\frac{1}{\sqrt{\frac{kR_s}{2}}|\phi_{nm} - \phi_{med}| - 1}\right] \tag{2.74}$$

where

$$R_s = \sqrt{(x_n - x_m)^2 + (z_n - z_m)^2}. \tag{2.75}$$

It is necessary to find the worst case (i.e., the maximum value of $\sqrt{R_s}|\phi_{nm} - \phi_{med}|$). The computation of $\sqrt{R_s}|\phi_{nm} - \phi_{med}|$ for all possible source-observation point sets would imply a cost of $O(N^2)$. For the most cases the terrain can be approximated by a coarser polygonal line with segments with dimensions proportional to the *strong group* G_s length. With this approximation, the minimum value of δ can be obtained by analyzing the saddle point distribution.

As it can be seen by inspection of Fig. 2.6, the central stretch C is limited by the cross point ϕ_1 with the steepest descent path of the saddle point $\phi_{s,min}$ (SDP$\phi_{s,min}$) and by the cross point ϕ_2 with the steepest descent path of the saddle point $\phi_{s,max}$ (SDP$\phi_{s,max}$). In most cases, the integrand will decay to zero near these points. However, for more complex terrains, when δ is close to 0^o, it may be possible that some contributions do not diminish enough along the stretch C, and so $F_n(\phi)$ may not decay to zero near the stretch extremes. Then, it would be necessary to add parts corresponding to portions of the SDP$\phi_{s,min}$ and SDP$\phi_{s,max}$. Considering that these points are placed close to the real axis, the SDPs can be approximated by 45^o straight lines.

In case the stretch L is needed for a correct integration, the stretch will be extended from ϕ_1 to ϕ_3, a point where the integrand decays to a reference value ζ. It is necessary to determine at which value of ϕ_3 the contribution of $\phi_{s,max}$ gets a value of ζ i.e.:

$$\mathrm{Im}(\phi_3) = -\sqrt{\frac{-\ln\zeta}{kL_s}} \tag{2.76}$$

where $Im(.)$ represents the imaginary part. In general a value of $\zeta = 10^{-3}$ provides a good accuracy in the complex integration, even though smaller values can be used.

An analogous procedure is used to determine the addition of the stretch R considering the saddle point placed as $\phi_{s,max}$.

2.4.4 Step of Integration

Once the path is determined, it is necessary to define the step of integration. For the central stretch C, the step of integration is defined as:

$$\Delta\phi_C = \sqrt{5/kR_{s,max}}/22 \tag{2.77}$$

where $R_{s,max} = \sqrt{L_s^2 + (z_{max} - z_{min})^2}$. This integration step could be used for the complete integration path, but the integrand over the lateral stretches smoothly decays to zero and a larger integration step could be used.

To determine the step used for the lateral stretches the distance $R_{s,max}$, in (2.77), must be substituted by the distance that defines the most significant saddle points over the lateral stretches. For the stretch L, the distance $R_{max,\phi_{s,min}}$ is the maximum distance between any pair of source-receiving points whose saddle point is placed at $\phi_{s,min}$. Meanwhile, for the stretch R, the distance $R_{max,\phi_{s,max}}$ is the maximum distance between any pair of source-receiving points whose saddle point is placed at $\phi_{s,max}$. This means that the steps of integration are taken as the following: for the stretch L

$$\Delta\phi_L = \sqrt{5/(kR_{max,\phi_{s,min}})}/22, \tag{2.78}$$

for the lateral stretch R

$$\Delta\phi_R = \sqrt{5/(kR_{max,\phi_{s,max}})}/22. \tag{2.79}$$

Then, the integration variable is mapped to the $Re(\phi)$ axis according to

$$d\phi_C \rightarrow \Delta\phi_C e^{j\delta} \tag{2.80}$$

$$d\phi_{L,R} \rightarrow \Delta\phi_{L,R} e^{j\pi/4}. \tag{2.81}$$

Spectral acceleration algorithm is very efficient for computing scattered fields when the terrain profile does not involve large height variations. As the height variation increases, the inclination angle δ takes very low values such that the path of integration will be so close to the real axis and the integrand will present very fast oscillations. In addition, the deformed contour of integration approaches

to its intersection with the SAP of the outermost saddle point. This point has a significant effect on the exponential growth of the integrand on the complex space. This implies that (2.74) is not valid anymore. In other words, the angular spectral integration path cannot be deformed in the complex angular plane. A great number of numerical tests on the SA-FBM over terrain profiles show that when the inclination angle δ is smaller than 4 degrees [30], weak region contribution does not converge and leads to inaccurate results. This makes the performance of SA-FBM highly dependent on geometry. That is why SA-FBM cannot be a reference solution when the terrain profile involves large height variations.

To remedy this problem, a hybrid approach which combines the characteristic basis function method with the physical optics solution (when applicable) and the forward-backward method has been developed for accurate and efficient solution of electromagnetic scattering and propagation problems that involve large scale and rough terrains. This new approach is discussed in the next chapter.

Chapter 3

Characteristic Basis Function Method

The FBM has been shown to provide a more rapid convergence than a standard non-stationary iterative algorithm in many cases. However, the FBM results in an operational count of $O(N^2)$ in the matrix vector multiplication, and in order to avoid $O(N^2)$ memory storage, a time consuming computation of the impedance matrix elements needs to be repeated on every iteration. This computational cost prohibits the application of the FBM to large-scale scattering problems. On the other hand, the Spectral Acceleration Forward-Backward Method (SA-FBM) is very efficient when it is applied to slightly rough such as ocean-like surfaces. Lopez *et al.* modified the integration contour of the method in order to implement SA-FBM to very undulating rough surfaces such as terrain profiles [13]. However, as the roughness of the profile is further increased, the spectral acceleration algorithm fails to provide accurate results owing to convergence problems during the computation of the weak region contribution. For terrain profiles with large height variations, it may not be possible to define integration paths in the complex plane avoiding sudden exponential growths of the integrand. It is claimed that by broadening the range of the plane wave expansion, such problems might be avoided. This claim will be reinvestigated. However, for the time being, large height variations make the method impractical and highly dependent on the

geometry.

Characteristic Basis Function Method (CBFM) which is first proposed by Prakash and Mittra in [14], aims to reduce the size of the matrix arising in the MoM formulation, using high level basis functions, called *characteristic basis functions (CBFs)*, defined on macro-domains by aggregating low-level (i.e., conventional sub-domain) basis functions. CBFM differs from the other entire-domain approaches in several aspects. First, the technique is more general, and can be applied to an arbitrary geometry; second, it includes the mutual interaction effects rigorously and systematically; third, it leads to small-size matrix systems that can be solved directly without any need to iterative solvers. The third aspect makes CBFM an iteration-free method.

3.1 CBFM Formulation For Terrain Profiles

The MoM formulation for the electromagnetic scattering problem results in a set of linear system of algebraic equations that are cast in a matrix form as follows

$$\mathbf{V} = \bar{\mathbf{Z}}\,\mathbf{I} \tag{3.1}$$

where $\bar{\mathbf{Z}}$ is the known MoM impedance matrix of size $N \times N$, $\mathbf{V}$ is an $N \times 1$ known excitation vector, and $\mathbf{I}$ is the unknown solution vector of size $N \times 1$.

CBFM approach starts with partitioning the terrain profile into M distinct blocks with N_i being the number of unknowns in block i (i.e., $\sum_{i=1}^{M} N_i = N$). For the sake of illustration, a terrain profile which is divided into M blocks is shown in Fig. 3.1. Next step is to construct a set of high-level basis functions that represent each block (a portion of the terrain profile). These characteristic basis functions (CBFs) are comprised of (i) primary basis functions (PBFs) arising from the self-interactions within the domain, and (ii) secondary basis functions (SBFs) that account for the mutual coupling effects from the rest of the domains. However, to eliminate the spurious edge effects at block truncations, each block is extended in both directions by Δ and hence, each extended block has N_i^e unknowns ($N_i^e > N_i$). Each CBF, whether a PBF or a SBF will represent the

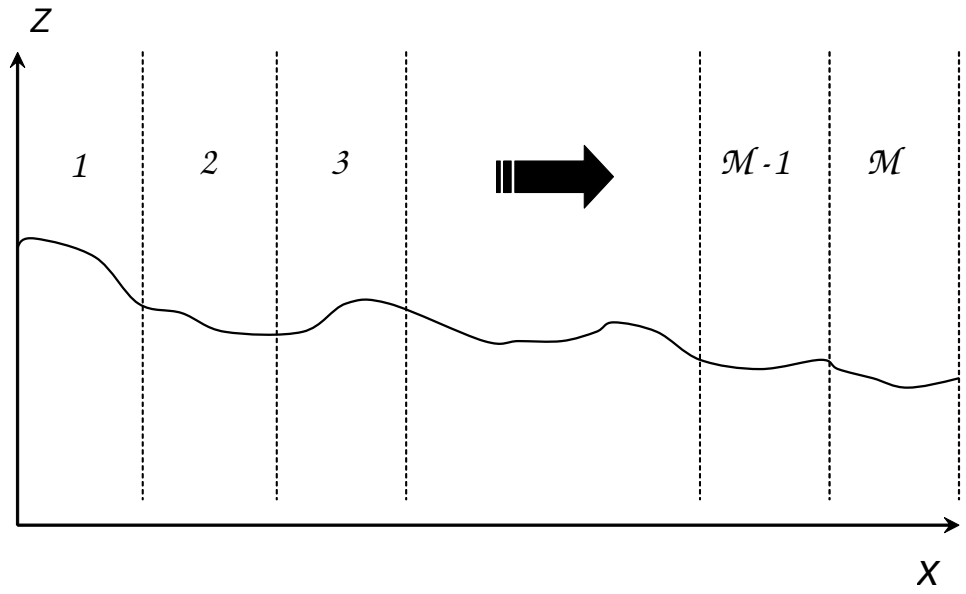

Figure 3.1: Geometry of a terrain profile partitioned into M blocks

entire block. Thus, the PBFs, denoted by $\mathbf{I}_i^{(i)}$, are constructed for each extended block by solving the equation

$$\bar{\mathbf{Z}}_e^{(i)}\ \mathbf{I}_i^{(i)} = \mathbf{V}^{(i)} \text{ for } i = 1, 2, ..., M \tag{3.2}$$

where $\bar{\mathbf{Z}}_e^{(i)}$ is the $N_i^e \times N_i^e$ self impedance matrix of the extended block i and $\mathbf{V}^{(i)}$ is the $N_i^e \times 1$ excitation vector corresponding to this block, which is a subset of $\mathbf{V}$ that includes the rows belonging to block i. The concept of block matrices is illustrated symbolically in Fig. 3.2, with $M = 3$, and the extended blocks are also shown in the same figure. The individual blocks are shown in solid lines, while the extended blocks are shown in dotted lines. Even though the original number of unknowns N may be quite large because the original terrain geometry is large in terms of the wavelength, the number of unknowns in each block (i.e., N_i) can be kept to a manageable size and hence, (3.2) can be solved using direct inversion techniques or iteratively leading to a computational cost of $O(N_i^3)$ or $O(N_i^2)$, respectively, for each block. In addition, since these PBFs will serve as a part of the basis functions to construct the reduced matrix, their accurate evaluation (particulary for large scale terrain geometries) is not necessary at this stage. Therefore, (3.2) is solved using single iteration of FBM to accelerate the method. Note that, depending on the nature of the electromagnetic source, that

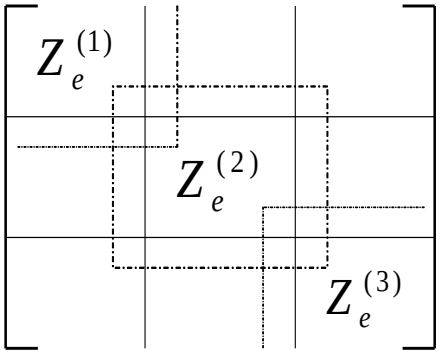

Figure 3.2: A three block segmentation of the MoM matrix

is used to illuminate the terrain profile, one can also use physical optics (PO) given by $\mathbf{J}_s^{PO} = 2\hat{n} \times \mathbf{H}^{inc}$ to construct PBFs. Use of PO obviously eliminates the need to solve (3.2). In this study, PBFs are found by using either a single iteration of FBM or PO to accelerate the method. It has been observed that, if the terrain is illuminated by an isotropic radiator or by a plane wave, then one can safely use PO. However, if the terrain is illuminated by a directive antenna (for instance a dipole) located at a couple of wavelengths above the terrain, then use of PO yields a visible deterioration on induced current results that also affects the accuracy of the scattered field. At the end of this step, M PBFs are generated.

Once the PBFs have been obtained, the next step is to construct the SBFs that account for the mutual interactions between the blocks. Following the procedure outlined in [14], fields due to the kth PBF evaluated on the ith block yield the excitation vector $\mathbf{V}_k^{(i)}$, to be used in the computation of the kth SBF for block i, $\mathbf{I}_k^{(i)}$, and is computed via the following matrix multiplication:

$$\mathbf{V}_k^{(i)} = -\bar{\mathbf{Z}}^{(i,k)}\mathbf{I}_k^{(k)} \tag{3.3}$$

where $\bar{\mathbf{Z}}^{(i,k)}$ is formed from the original MoM matrix $\bar{\mathbf{Z}}$ by selecting the testing location at the extended block i, with the source location being the block k. If the extended block i shares a number of unknowns, let's say $N_{i,k}^c$, with block k, then by eliminating these source locations, the sizes of $\bar{\mathbf{Z}}^{(i,k)}$ and $\mathbf{I}_k^{(k)}$ become $N_i^e \times (N_k - N_{i,k}^{(c)})$ and $(N_k - N_{i,k}^{(c)}) \times 1$, respectively. On the other hand, if the

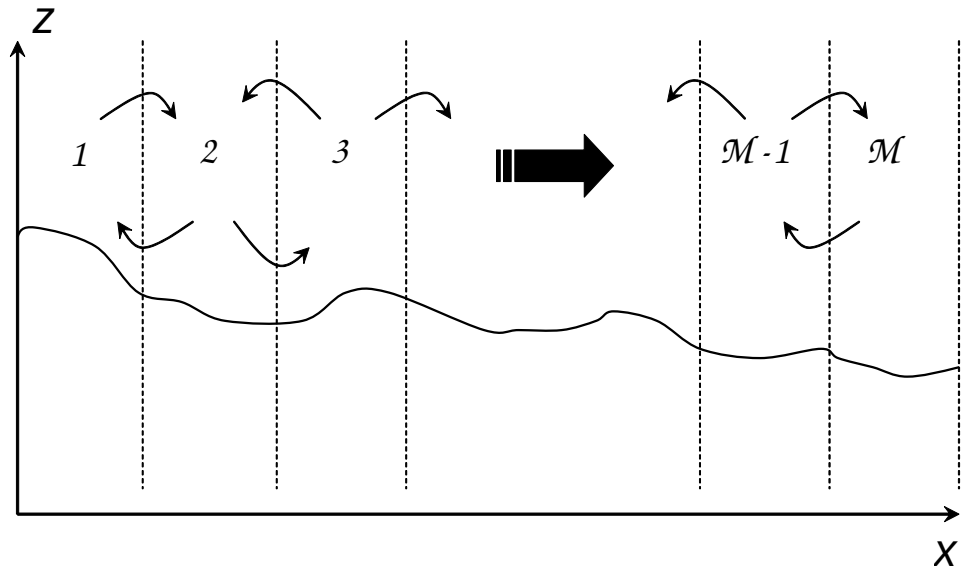

Figure 3.3: Illustration of mutual interactions between neigbouring blocks

extended block i and block k are far-away blocks (i.e., there is no overlap due to extension of the blocks), then the sizes of $\bar{\mathbf{Z}}^{(i,k)}$ and $\mathbf{I}_k^{(k)}$ become $N_i^e \times N_k$ and $N_k \times 1$, respectively. After evaluating $\mathbf{V}_k^{(i)}$ from (3.3), the SBF for block i, $\mathbf{I}_k^{(i)}$, is found from the solution of

$$\bar{\mathbf{Z}}_e^{(i)} \; \mathbf{I}_k^{(i)} = \mathbf{V}_k^{(i)}. \tag{3.4}$$

Similar to PBFs, accurate evaluation of SBFs is not required at this stage and hence, single iteration of FBM is used in (3.4) to ensure efficiency. Note that in $1-D$ terrain problems it is expected that the SBFs of well-separated groups will be very similar to the SBFs of adjacent groups. Therefore, in contrast to [14], only the mutual interactions between the adjacent blocks are retained as illustrated in Fig. 3.3 (i.e., for block i, SBFs are constructed for blocks $k = i-1$ and $k = i+1$). This is mainly due to the fact that, in an electrically large terrain, mutual interactions among the far-away blocks are very weak. Therefore, the sizes of $\bar{\mathbf{Z}}^{(i,k)}$ and $\mathbf{I}_k^{(k)}$ used in (3.3) are generally $N_i^e \times (N_k - N_{i,k}^{(c)})$ and $(N_k - N_{i,k}^{(c)}) \times 1$, respectively. Also note that the two end-blocks have single SBFs. Consequently, the total number of SBF turns out to be $2M-2$ leading to a total of $3M-2$ CBFs (M PBFs + $2M-2$ SBFs) for terrain problems. At this point, it should be mentioned that if more SBFs are included (i.e., more neighboring blocks are

included on each side of the extended block i), the accuracy of the solution (taking FBM as a reference solution) improves up to a certain degree and then remains the same. However, such an improvement in the accuracy is not uniform throughout the terrain. It is usually more dominant close to the source region. Unfortunately, for extremely large terrains it brings significant computational burden and memory requirements during the construction of the reduced matrix, which is to be explained next.

After constructing all CBFs, the solution to the entire problem is expressed as a linear combination of $3M-2$ CBFs (under the assumption that only the adjacent blocks are included during the construction of the SBFs) given by

$$\mathbf{I}_{N\times 1} = \sum_{k=1}^{2} \alpha_k^{(1)} \begin{bmatrix} [\mathbf{I}_k^{(1)}] \\ [0] \\ . \\ . \\ [0] \end{bmatrix} + \sum_{k=1}^{3} \alpha_k^{(2)} \begin{bmatrix} [0] \\ \left[\mathbf{I}_k^{(2)}\right] \\ . \\ . \\ [0] \end{bmatrix} + ... + \sum_{k=1}^{2} \alpha_k^{(M)} \begin{bmatrix} [0] \\ [0] \\ . \\ . \\ \left[\mathbf{I}_k^{(M)}\right] \end{bmatrix} \quad (3.5)$$

where $\alpha_k^{(i)}$ is the unknown complex expansion coefficient for the kth basis function of block i. Substituting (3.5) into (3.1), the solution can be cast into the following form:

$$\mathbf{V}_{N\times 1} = \sum_{k=1}^{2} \alpha_k^{(1)} \mathbf{u}_k^{(1)} + \sum_{k=1}^{3} \alpha_k^{(2)} \mathbf{u}_k^{(2)} + ... + \sum_{k=1}^{3} \alpha_k^{(M-1)} \mathbf{u}_k^{(M-1)} + \sum_{k=1}^{2} \alpha_k^{(M)} \mathbf{u}_k^{(M)} \quad (3.6)$$

where

$$\mathbf{u}_k^{(i)} = [[\bar{\mathbf{A}}_{1,i}\ \mathbf{I}_k^{(i)}][\bar{\mathbf{A}}_{2,i}\ \mathbf{I}_k^{(i)}]...[\bar{\mathbf{A}}_{M,i}\ \mathbf{I}_k^{(i)}]]^T\ . \quad (3.7)$$

Note that in (3.7) $\bar{\mathbf{A}}_{i,k}$ is the MoM impedance matrix in (3.1), and generated selecting observation points in block i and source points in block k. It differs from $\bar{\mathbf{Z}}^{(i,k)}$ used in (3.3) in the sense that $\bar{\mathbf{A}}_{i,k}$ is not an extended matrix since the extension parts are truncated prior to (3.5). To solve (3.6), the inner product of both sides is taken with the Hermitian of each $\mathbf{u}_k^{(i)}$ given by (3.7) to generate the $(3M-2)\times(3M-2)$ reduced matrix. The solution of the resultant matrix equation yields the unknown expansion coefficients, $\alpha_k^{(i)}$, for the CBFs. Note that accurate solution of the reduced matrix equation is now critical and direct solvers are preferred. In fact, the direct solution of this system does not pose a computational

burden since $3M-2$ is significantly small compared to N. Moreover, even for cases where $3M-2$ is large, one can use recently developed direct solvers that can handle up to million unknowns [34] or reformulate the problem so that multilevel CBFM [22], that makes the direct solution for the corresponding reduced matrix feasible, can also be implemented.

Extrapolation Process

The most time-consuming and main memory-intensive parts of the method are the storage of $\mathbf{u}_k^{(i)}$ given by (3.7) and the generation of the reduced matrix regardless of using FBM (or PO) in the construction of CBFs. However both the computation time and the memory requirements can be significantly reduced using a very simple extrapolation process. Notice that the vectors, $\mathbf{u}_k^{(i)}$, actually represent the entire domain fields of the induced current $\mathbf{I}_k^{(i)}$ on the entire ith block. It is observed that in many regions of a large scale terrain profile these field amplitudes vary slightly and their phase variation is almost linear as shown in Fig. 3.4. Hence, during the generation of (3.7), relatively small groups are formed from the elements of $\mathbf{u}_k^{(i)}$ in such a way that the roughness of regions along the terrain governs the number of elements in each group. Abrupt roughness variations are usually selected as the borders of these groups. Practically, groups can be composed of 20, 50 or in some cases 100 elements. Then, assuming linearly varying phase and constant amplitude for the fields (i.e., elements of $\mathbf{u}_k^{(i)}$) within each group, two elements at the middle are chosen, the phase difference between them is computed, and the values of the remaining elements in the group are determined via simple extrapolation when needed. As a result, for a group of $2l$ elements (l may vary from group to group), a factor of l is defined to indicate the amount of acceleration in the computation time and the savings from the memory requirements. Although this extrapolation procedure requires a modest amount of pre-processing, it is easy to implement, and it can accelerate the method by a factor of L_{eff} (effective reduction factor), which is given by

$$L_{eff} = \left(\frac{\sum_{i=1}^{N_g} \frac{\Delta x_i}{l_i}}{x_{total}} \right)^{-1} \tag{3.8}$$

where N_g is the total number of groups, Δx_i is the length of each group and

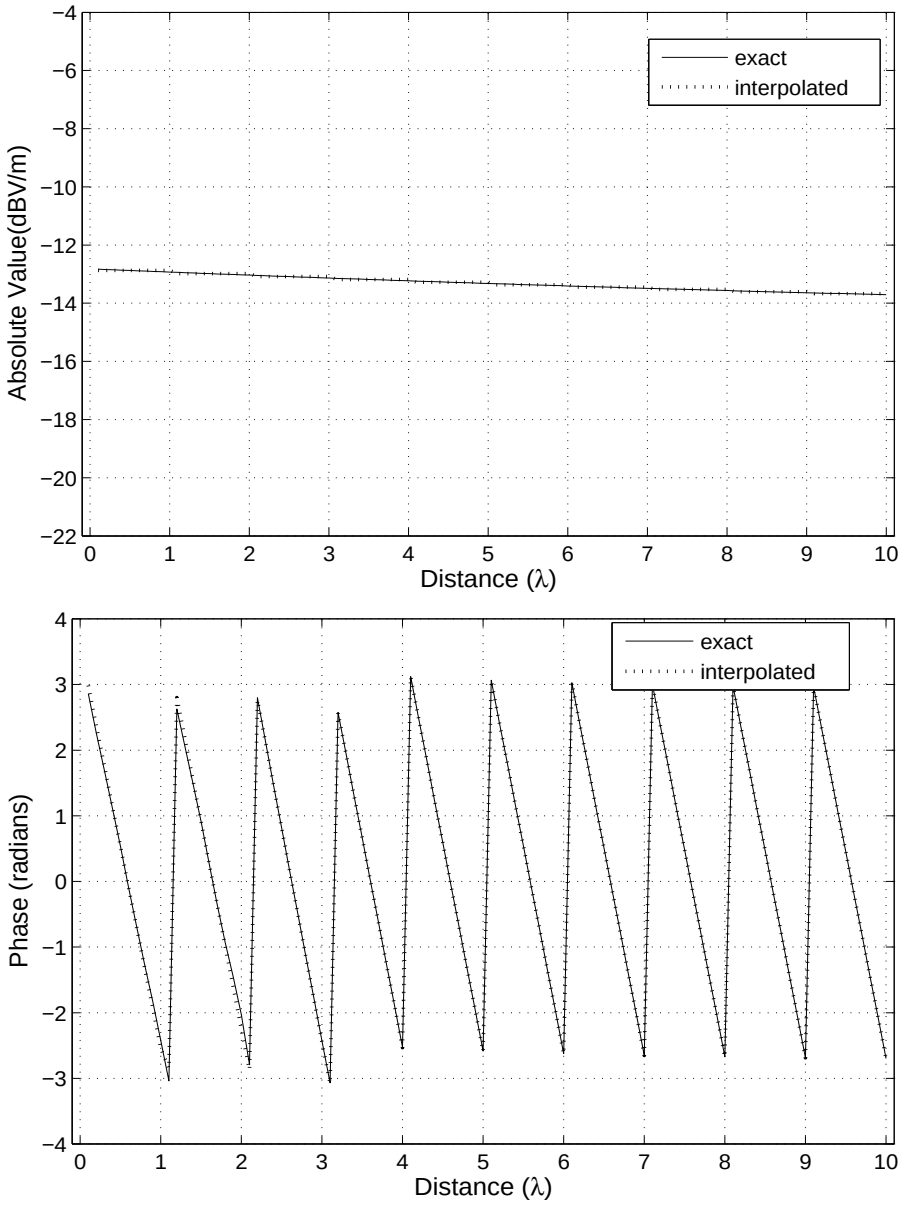

Figure 3.4: A 10λ portion of a $\mathbf{u}_k^{(i)}$ vector and its extrapolated version with L_{eff}=10

x_{total} is the length of the whole terrain. L_{eff} is usually between 10 and 20 for the real-life terrain profiles considered in this study.

Computation of the Scattered Field

Once the current distribution over the rough surface profile has been computed, the next step is to compute the scattered field. If the region of interest corresponds to a small portion of the surface, the numerical evaluation of the total field will involve a reduced number of operations. But if these regions are extended to the complete terrain profile and the field strength is computed in a dense set of points, similar to the MoM discretization, the CPU cost will increase up to $O(N^2)$, since the scattered field is expressed as,

$$\begin{aligned} E_y^{scat}(\boldsymbol{\rho}_n) &= -j\omega A_y - \frac{1}{\epsilon}\left(\frac{\partial F_x}{\partial z} - \frac{\partial F_z}{\partial x}\right) \\ &\cong -\frac{\omega\mu}{4}\sum_{m=1}^{N} I_m \Delta x_m H_0^{(2)}(k|\boldsymbol{\rho}_n - \boldsymbol{\rho}_m|) \\ &-j\frac{k}{4}\sum_{m=1}^{N} I_m \Delta x_m \eta_m H_1^{(2)}(k|\boldsymbol{\rho}_n - \boldsymbol{\rho}_m|)\hat{n}_m \cdot \hat{p}_{nm} \end{aligned} \tag{3.9}$$

and

$$\begin{aligned} H_y^{scat}(\boldsymbol{\rho}_n) &= -j\omega F_y + \frac{1}{\mu}\left(\frac{\partial A_x}{\partial z} - \frac{\partial A_z}{\partial x}\right) \\ &\cong \frac{\omega\epsilon}{4}\sum_{m=1}^{N} I_m \Delta x_m \eta_m H_0^{(2)}(k|\boldsymbol{\rho}_n - \boldsymbol{\rho}_m|) \\ &+j\frac{k}{4}\sum_{m=1}^{N} I_m \Delta x_m H_1^{(2)}(k|\boldsymbol{\rho}_n - \boldsymbol{\rho}_m|)\hat{n}_m \cdot \hat{p}_{nm} \end{aligned} \tag{3.10}$$

for TM and TE polarization cases respectively. In (3.9) and (3.10) I_m denotes the computed induced current on the source point $\boldsymbol{\rho}_m$, and $\boldsymbol{\rho}_n$ denotes the observation point where the scattered field will be obtained.

Chapter 4

Numerical Results

In this chapter, numerical results are presented to validate the efficiency and accuracy of CBFM over different one-dimensional terrain profiles. Results are obtained for both horizontal (i.e., TM) and vertical (i.e., TE) polarizations. In all results, a point-matching with rectangular pulse-shaped basis functions that have $\lambda/10$ pulse width has been utilized. In order to check the accuracy of the method, results are compared with the FBM and the SA-FBM, if applicable.

The first set of results are given to test the accuracy of the proposed method on a relatively smooth terrain as illustrated in Fig. 4.1(a). The terrain is a 2000λ (i.e., $N = 20000$) non-PEC rough surface profile with $\eta_s = 20 + j20$. Solid line represents the surface profile whereas dashed line represents 1.8λ above the surface, where the field distribution is going to be computed. This surface is illuminated by a dipole antenna which is considered to be 25 Watts and located at a height 25λ above the beginning of the surface ($x_1 = 0$, $z_1 = 25\lambda$). For horizontal polarization, elements of the incident field vector can be given by,

$$V_n = -E_y^{inc}(\boldsymbol{\rho}_n) = -E_0 \frac{e^{-jkd_n}}{d_n} \sin\theta_n \tag{4.1}$$

where θ_n is the elevation angle of the receiving element from the vertical axis of the source, and $\sin\theta_n$ can be determined by

$$\sin\theta_n = \frac{x_n - x_1}{d_n} \ . \tag{4.2}$$

In (4.2) d_n denotes the distance between the nth receiving element and the source. It is given by,

$$d_n = \sqrt{[x_n - x_1]^2 + [z_n - z_1]^2}. \tag{4.3}$$

For vertical polarization, elements of the incident field vector is given by,

$$V_n = -H_y^{inc}(\boldsymbol{\rho}_n) = -\frac{E_0}{\eta_0}\frac{e^{-jkd_n}}{d_n}\,\sin\theta_n. \tag{4.4}$$

Using the radiation intensity integral in [35], the transmitted power from the dipole, P_t, is calculated from,

$$P_t = \int_{\theta=0}^{\pi}\int_{\phi=0}^{2\pi}\frac{|E_0|^2}{2\eta}\,\sin\theta d\theta d\phi\ , \tag{4.5}$$

and the magnitude of the electric field can be related to P_t as

$$E_0 = \sqrt{90P_t} \tag{4.6}$$

and is considered to be 25 Watts.

For this problem, operating frequency is chosen to be 300 MHz. Since the profile does not involve big height variations, SA-FBM is used as a reference solution. When applying CBFM, the terrain is partitioned into 100 blocks and 298 CBFs are used. During the generation of CBFs, single-iteration FBM is used. A uniform extrapolation is used for this terrain. Therefore, the acceleration factor l becomes L_{eff} and is chosen to be 50. Fig. 4.1(b) and Fig. 4.1(c) show the induced current magnitudes on the surface for TM polarization case when no extension is performed and 1λ extension is performed, respectively. As can be clearly seen in Fig. 4.1(b), when the blocks are not extended, the current distribution involves spurious edge effects. In Fig. 4.1 (c), it can be observed that these spurious edge effects are substantially reduced when 1λ extension is performed. Extensions beyond 1λ did not affect (i.e., improve) the accuracy. Therefore, for the rest of all results an extension of 1λ is used for the suppression of spurious edge effects. As a matter of fact, such edge effects do not create a visible problem on the accuracy of the field distribution as illustrated on Fig. 4.2(b) and 4.2(c). For both cases, the total field results are in perfect agreement with the SA-FBM results. Fig. 4.3 illustrates the induced current and total field results for TE polarization.

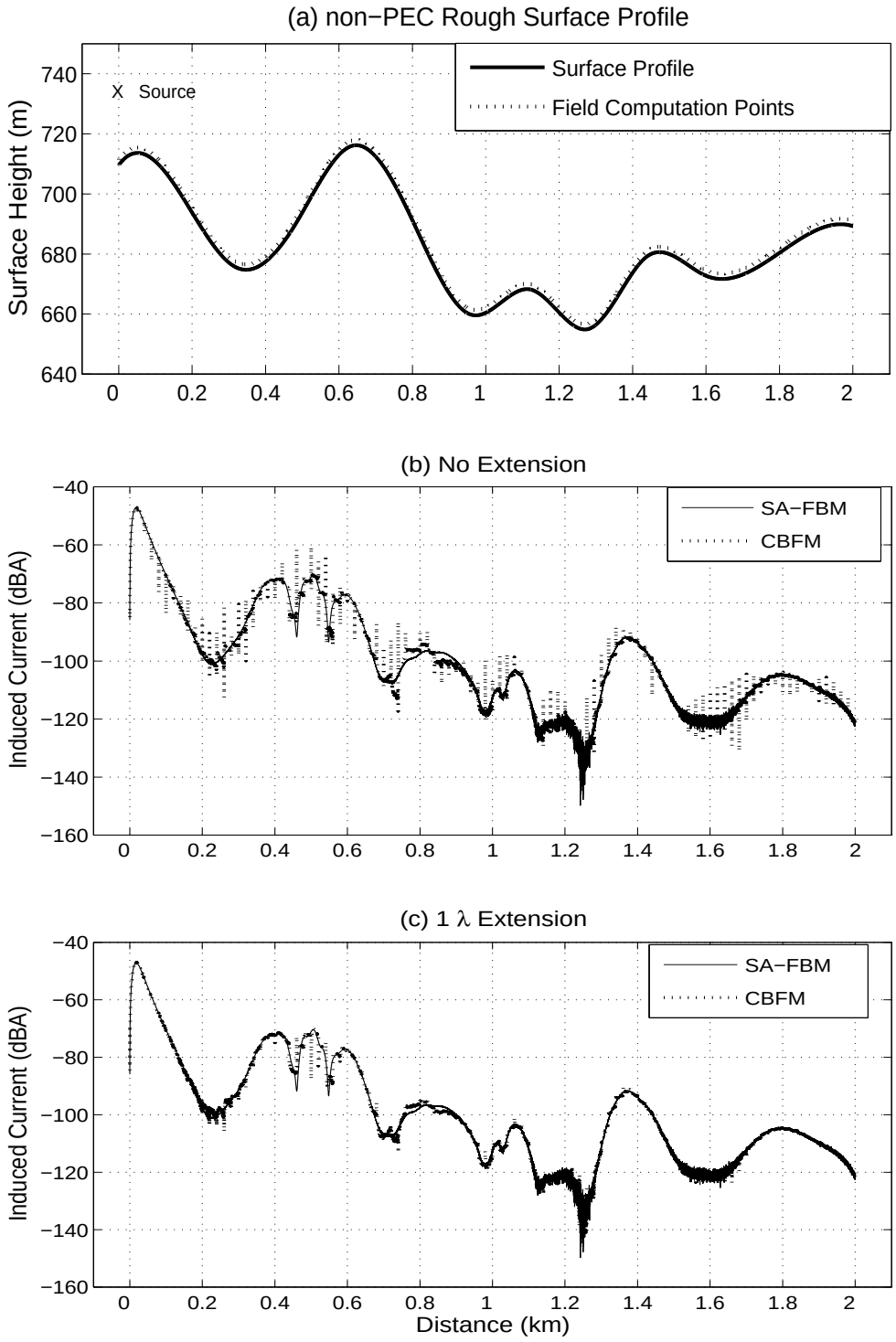

Figure 4.1: Induced current on a 2000 λ rough surface (TM polarized dipole). $M = 100$, $L_{eff} = 50$.

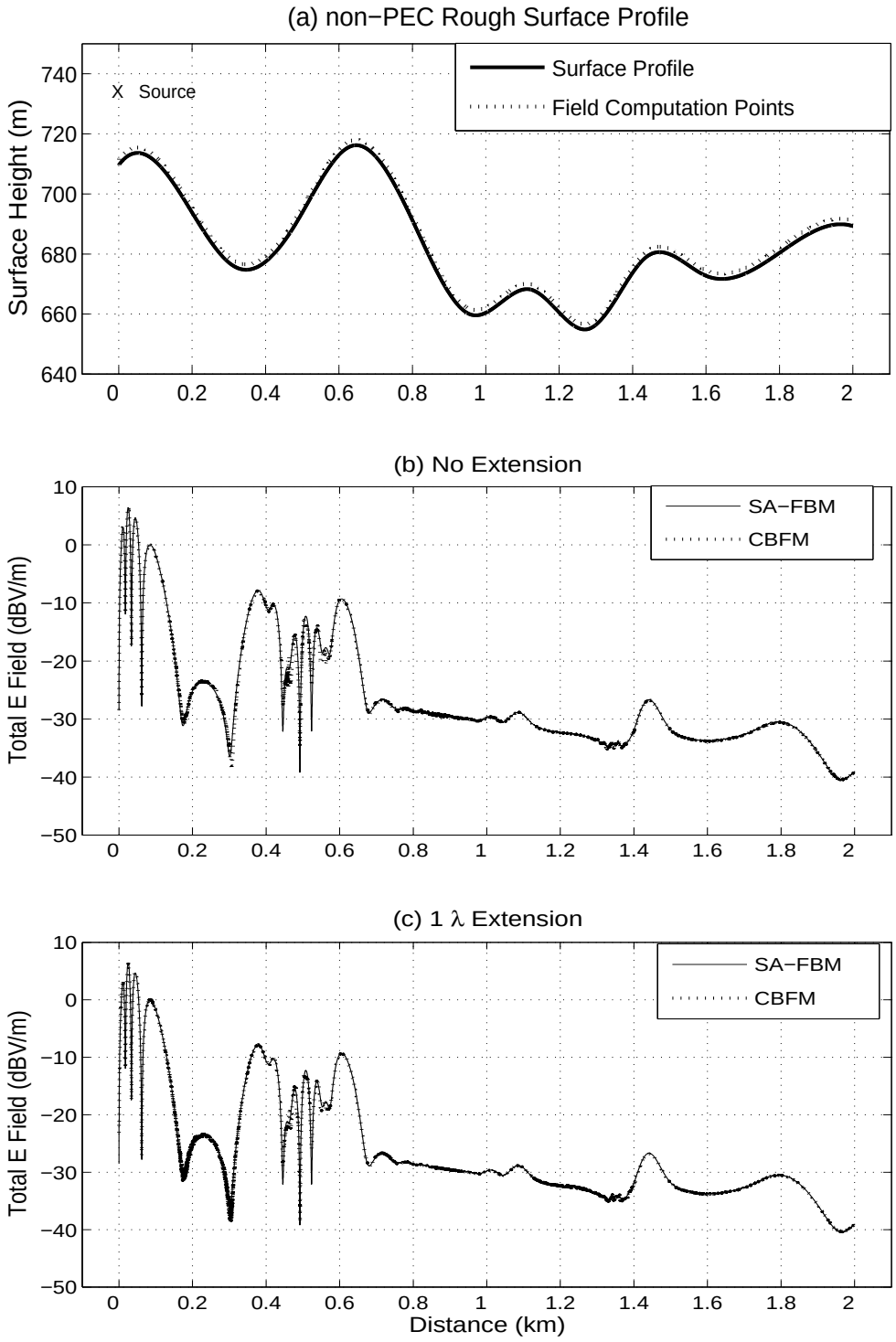

Figure 4.2: Total field above a 2000 λ rough surface (TM polarized dipole). $M = 100$, $L_{eff} = 50$.

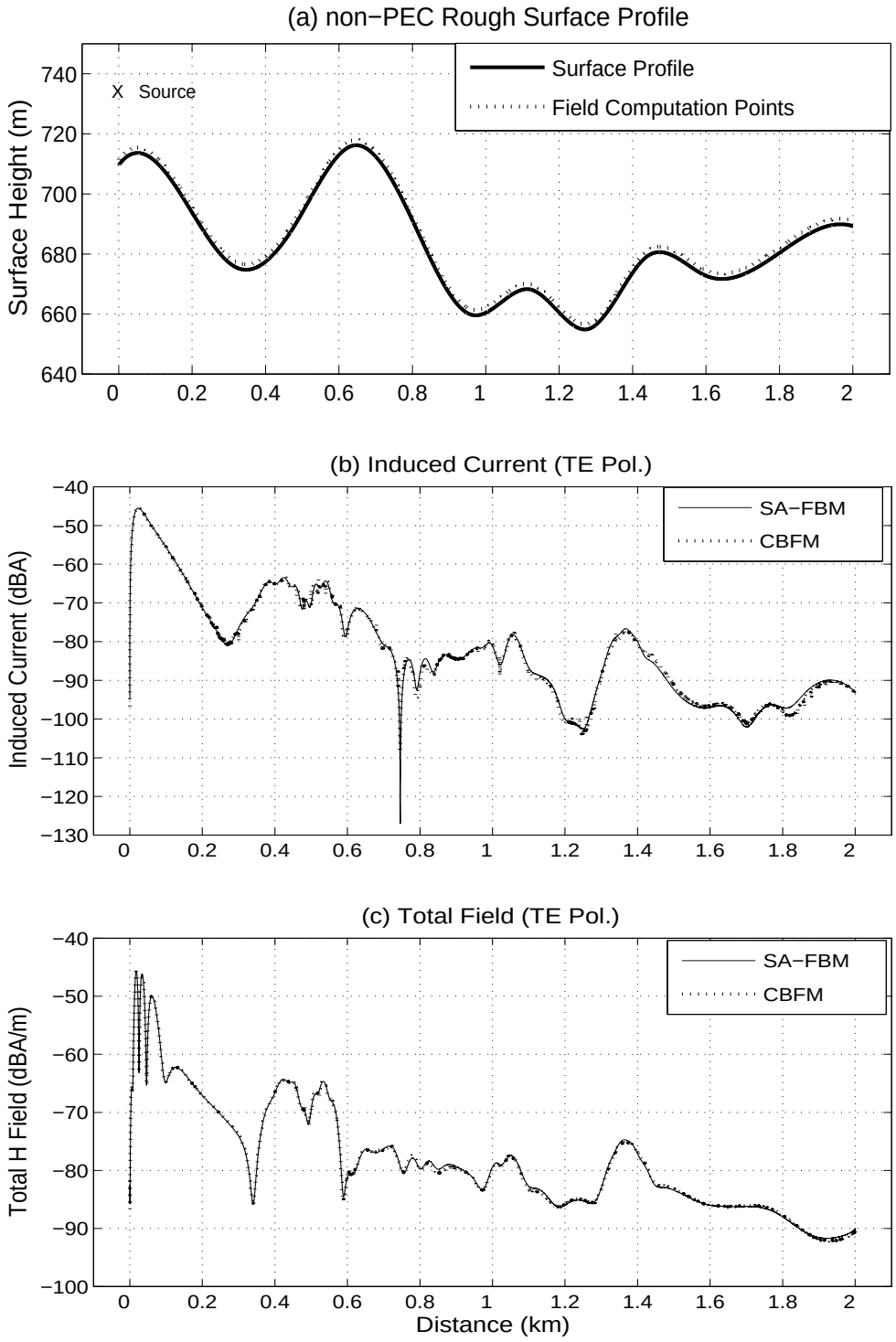

Figure 4.3: Induced current and total field results for a 2000 λ rough surface (TE polarized dipole). $M = 100$, $L_{eff} = 50$.

Fig. 4.4. (a) illustrates the same non-PEC rough surface profile given in Fig. 4.1. This time, terrain is illuminated by a grazing incident plane wave. For horizontal polarization, elements of the excitation vector become

$$V_n = -E_y^{inc}(\boldsymbol{\rho}_n) = e^{-jk(x_n \cos\theta - z_n \sin\theta)} \tag{4.7}$$

where θ is the angle of incidence from x-axis and is taken as $\pi/20$. For vertical polarization, elements of the excitation vector is given by

$$V_n = -H_y^{inc}(\boldsymbol{\rho}_n) = \frac{1}{\eta_0}\, e^{-jk(x_n \cos\theta - z_n \sin\theta)} \ . \tag{4.8}$$

For this problem, M is chosen to be 100 and during the generation of PBFs, PO is used and L_{eff} is chosen to be 50. SBFs are generated using single iteration FBM. Fig. 4.4 shows the induced current magnitudes and total field distribution for TM polarization and Fig. 4.5 shows the induced current and total field distribution for TE polarization. For both cases, CBFM results are in good agreement with the SA-FBM results. Therefore, we can conclude that CBFM approach yields accurate results for plane wave illumination, as well.

The next set of results are obtained over a real-life, 20 km downhill terrain profile around , as illustrated in Fig. 4.6(a). Operating frequency is 500 MHz, hence, total number of surface unknowns turns out to be 330000. Profile is considered to have an impedance surface of $\eta_s = 25 + j20\Omega$. At 500 MHz, this impedance corresponds to a relative permittivity of $\epsilon_r = 30.43$ and a conductivity of $\sigma = 3.76$.

The surface profile is assumed to be illuminated by an isotropic antenna with $P_t = 50W$, located at 25 meters above the left-most end of the surface, for both TM and TE polarizations. The total feld strengths are evaluated over a copy of each original terrain at $h = 1.8$ meters above. When applying CBFM, terrain is partitioned into 100 blocks. PBFs are generated via PO and only neighboring blocks are taken into account while generating SBFs. A uniform extrapolation process is performed over the entire surface, making $L_{eff} = 50$. SA-FBM is used as a reference solution since the terrain does not involve big height variations. Total field distributions for both TM and TE polarizations are given in Fig. 4.6(b) and (c), respectively.

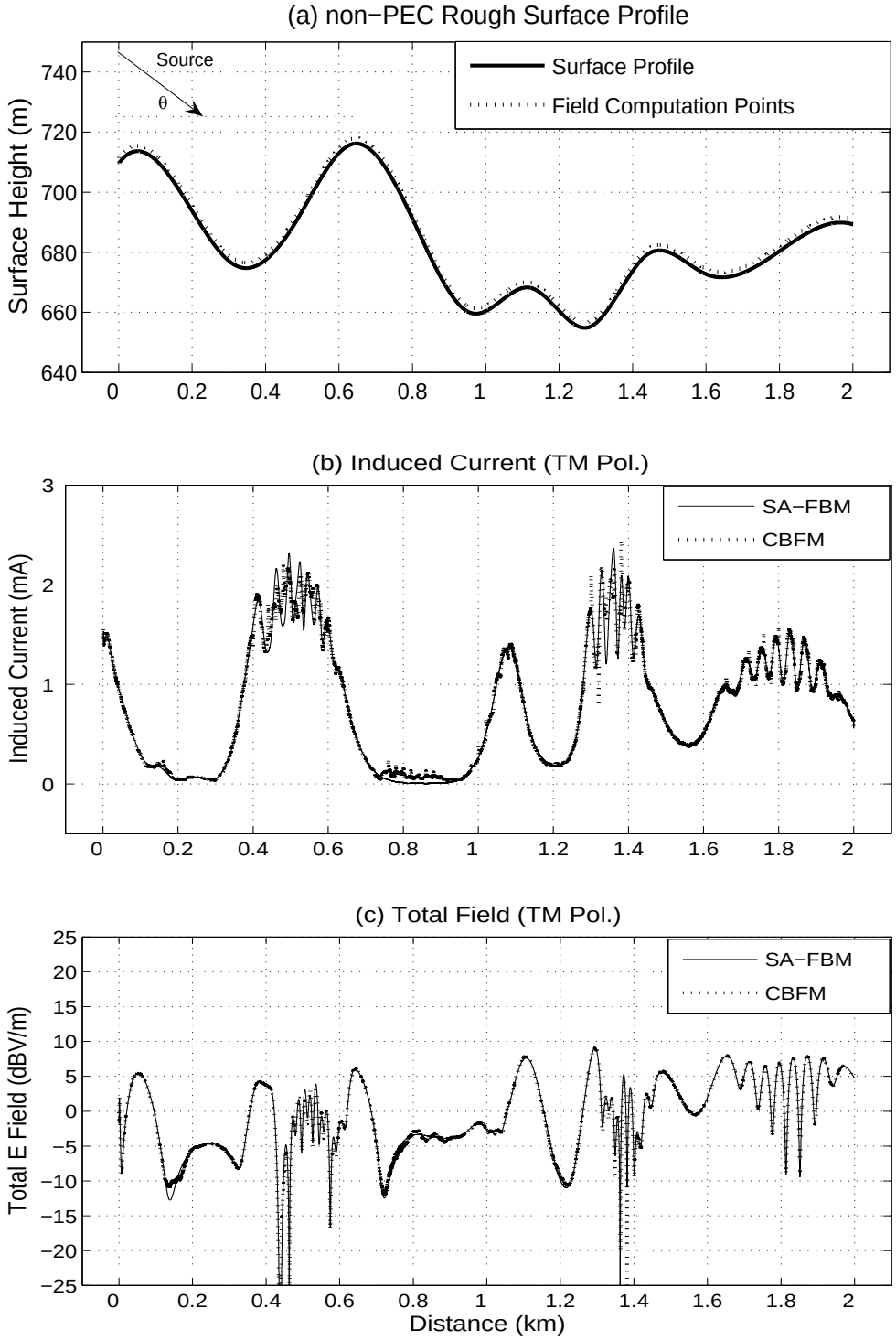

Figure 4.4: Induced current and total field results for low-grazing ($\theta = \pi/20$) TM polarized plane wave. $M = 100$, $L_{eff} = 50$.

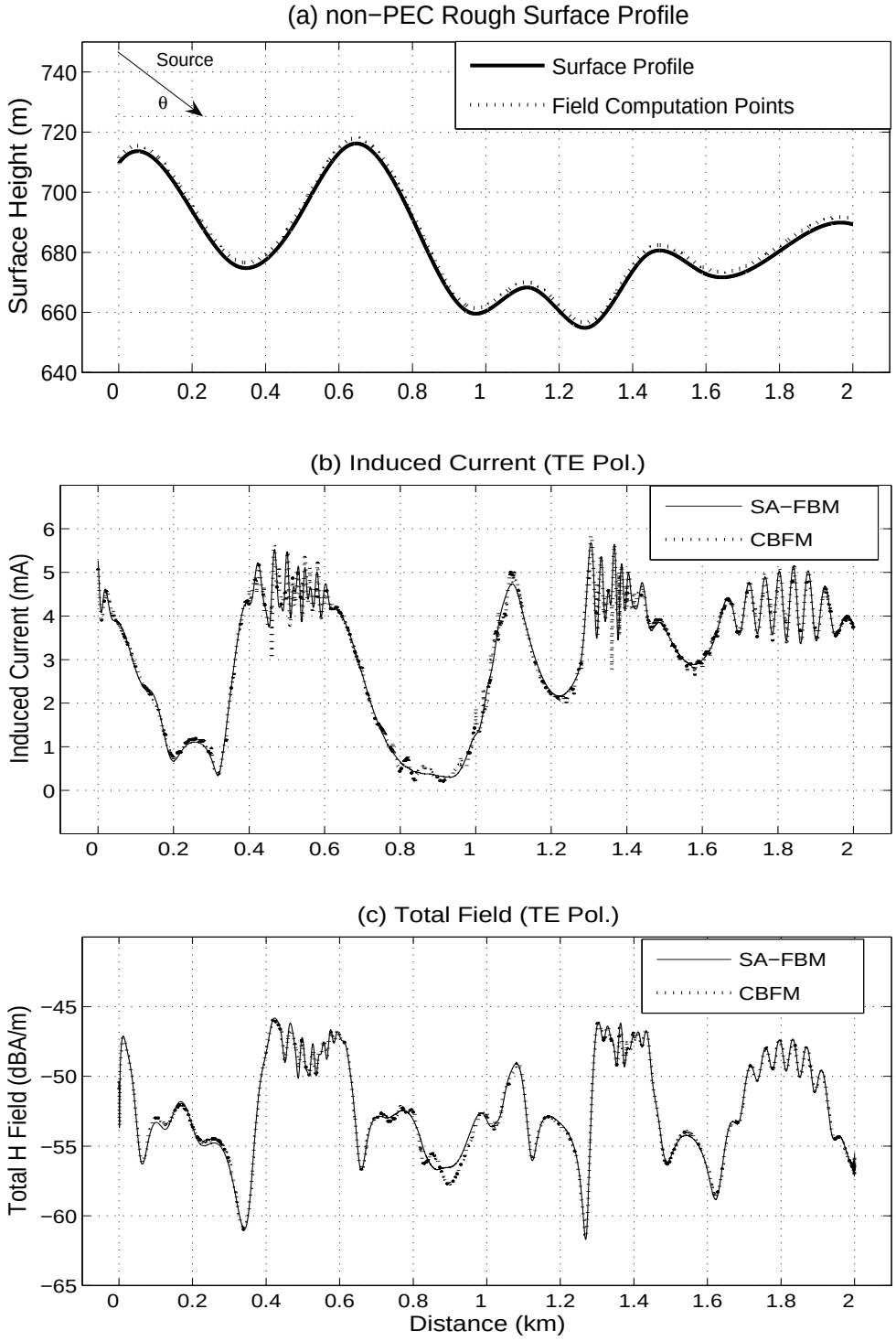

Figure 4.5: Induced current and total field results for low-grazing ($\theta = \pi/20$) TE polarized plane wave. $M = 100$, $L_{eff} = 50$.

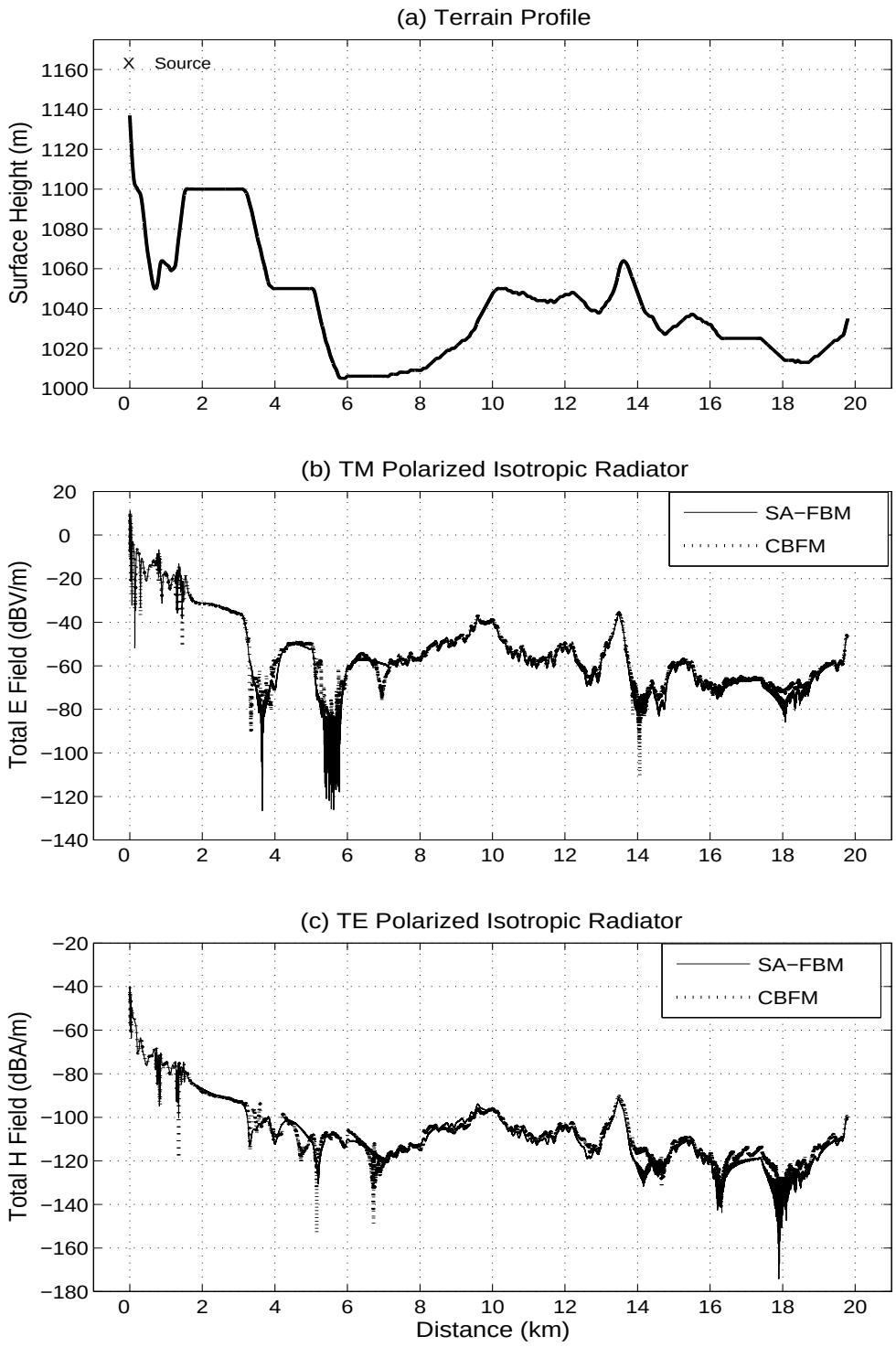

Figure 4.6: Total field results for TM and TE polarized isotropic radiator over a 20 km downhill profile near Ankara. $M = 100$, $L_{eff} = 50$.

The next set of results is the comparisons of CBFM with the measurements and the SA-FBM. The selected terrains, namely Hadsund and Jerslev terrain profiles in Fig. 4.7 (a) and Fig. 4.8 (a), respectively, are from Denmark. The measured data is obtained from [36], derived by using a transmitting dipole located at a height of 10.4 meters with a transmitted power of 10 Watts and a gain of 8 dBi. The receiving antenna is on the top of a van with a height of 2.4 meters. A surface impedance value $\eta_s = 20 + j8.1\Omega$ is used in order to handle some small forests and other types of land covers along the profiles. The path loss results for TM polarization at 435 MHz over Hadsund and at 970 MHz for Jerslev profiles are presented in Fig. 4.7 (b) and 4.8 (b), respectively. To generate the CBFM results, the Hadsund terrain, that is 7931 meters long ($N = 115000$), is divided into 100 blocks (i.e., $M = 100$) and 298 CBFs are used. The corresponding values for the 5446 meters long Jerslev profile are; $N = 180000$ at 970 MHz, $M = 100$ and the total number of CBFs is 298. In the generation of CBFs, PBFs and SBFs are obtained via a single iteration of FBM. A non-uniform extrapolation process, detailed in the previous section, is implemented to accelerate the generation of $\mathbf{u}_k^{(i)}$ vectors. The number l is selected to be large ($l = 50$) at relatively flat portions of the terrains, which correspond to 0-2 km range for the Hadsund terrain and 0.75-1.5 km for the Jerslev terrain, and $l = 10$ is used for the rest. As a result, $\mathbf{u}_k^{(i)}$ generation part of the method is accelerated by approximately 12.5 and 11 times, for the Hadsund and Jerslev terrain profiles, respectively. As seen in Fig. 4.7 (b) and in Fig. 4.8 (b), CBFM results are in good agreement with both measurements and SA-FBM that verifies the accuracy of the method. It is obvious that SA-FBM, being an $O(N)$ type method, is much faster than CBFM. However, it fails as the roughness of the terrain profile increases, particularly when there are large height variations along the terrain. Hadsund terrain profile considered here has a height variation less than 60 meters while it is 25 meters for the Jerslev terrain.

In the next set of results, effects of some parameters such as the number of blocks and the number of SBFs on the efficiency and accuracy of the method will be investigated in detail for terrain profiles with large height variations where SA-FBM fails to give accurate results.

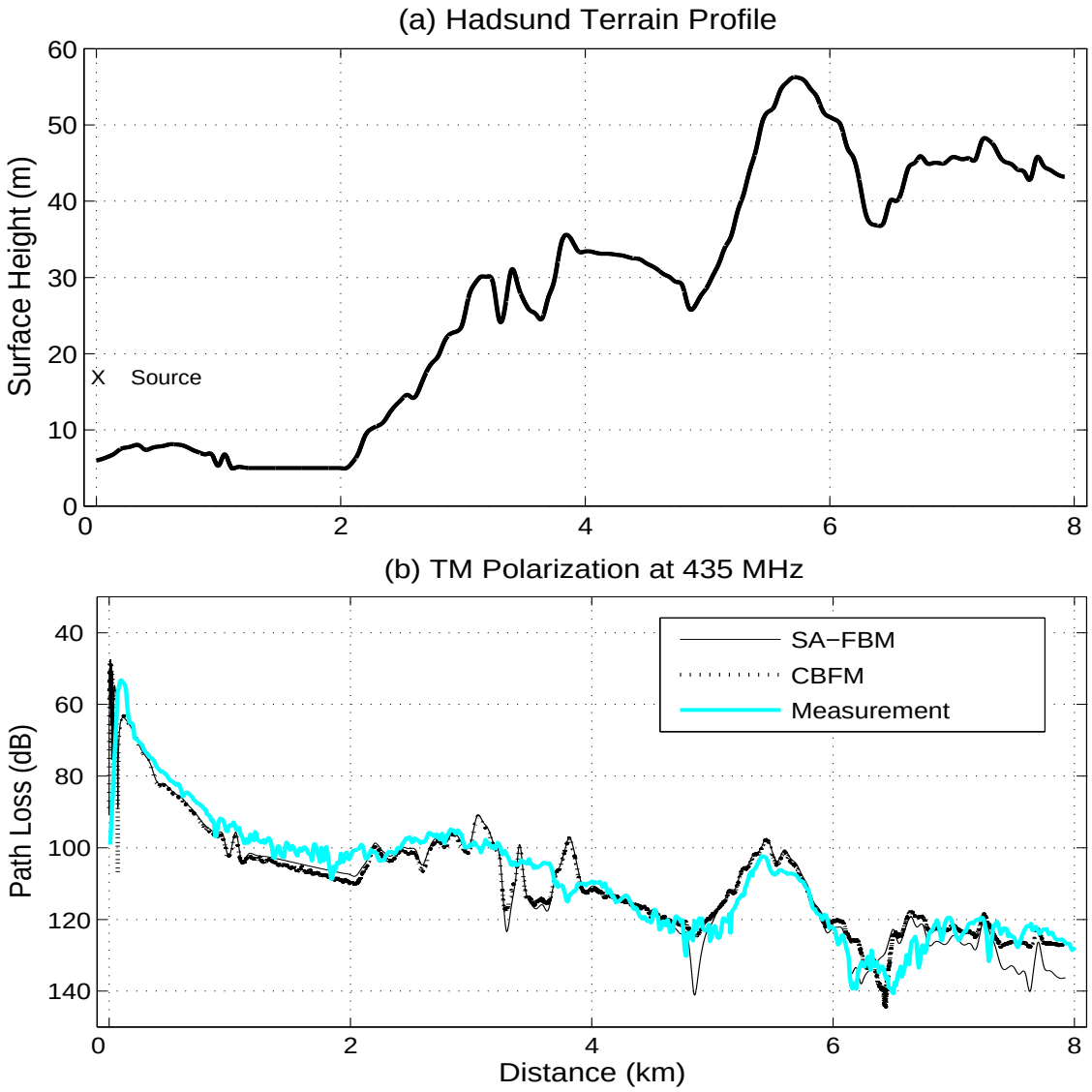

Figure 4.7: Path loss for TM polarized dipole over Hadsund terrain profile at 435 MHz. Distance 7931 m. $N = 115000$, $M = 100$, $L_{eff} = 12.5$.

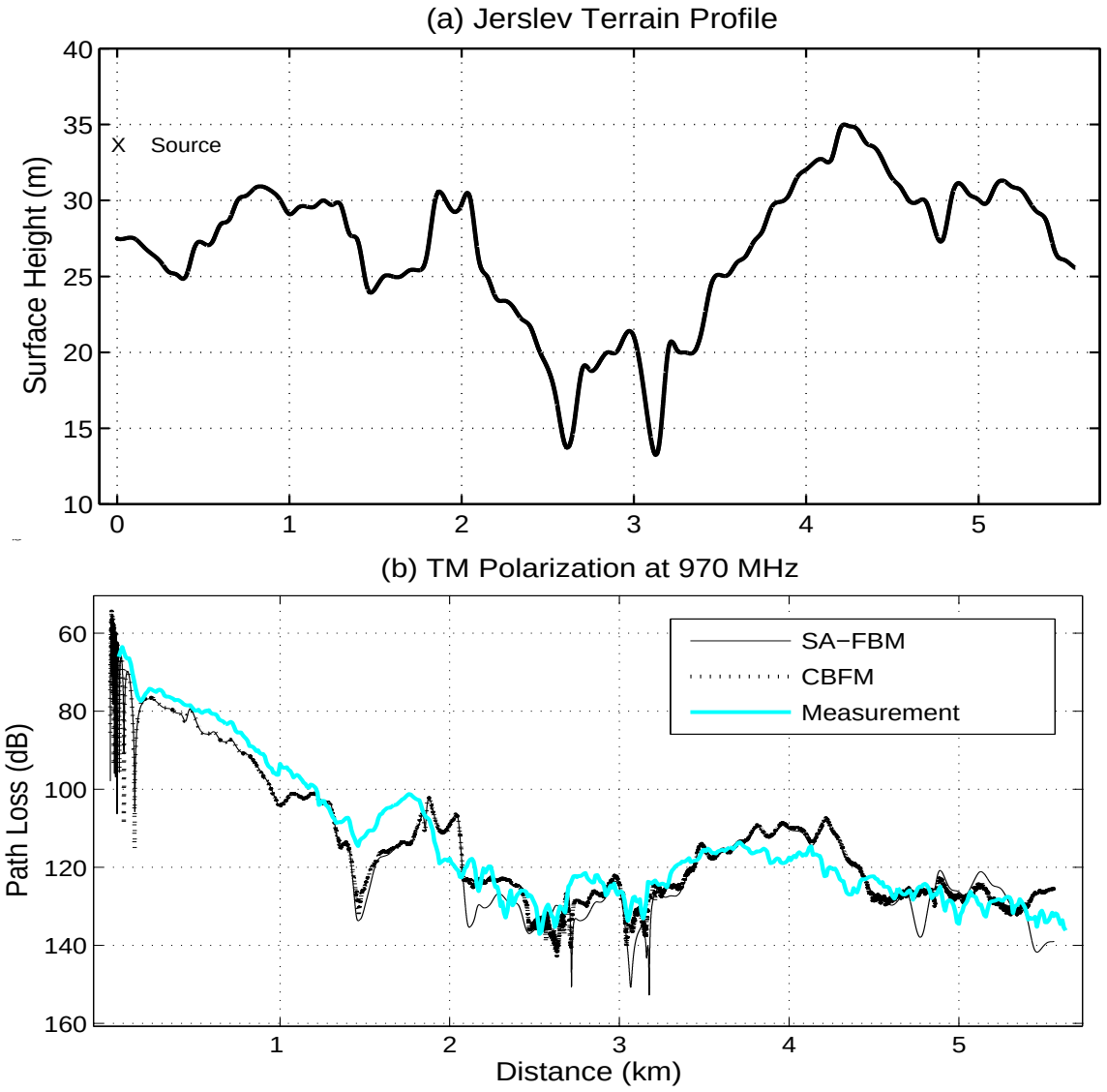

Figure 4.8: Path loss for TM polarized dipole over Jerslev terrain profile at 970 MHz. Distance 5446 m. $N = 180000$, $M = 100$, $L_{eff} = 11$.

Consider the surface profile illustrated in Fig. 4.9 (a). This terrain is a 5 km portion from the west side of Turkey with $\eta_s = 20 + j15$, and has a height variation more than 700 meters. The terrain is illuminated by an isotropic radiator with 25 Watts output. The elements of the excitation vector for the horizontal polarization is given by

$$V_n = -E_y^{inc}(\boldsymbol{\rho}_n) = -E_0 \frac{e^{-jkd_n}}{d_n} \ . \tag{4.9}$$

For vertical polarization, elements of the incident field vector is given by

$$V_n = -H_y^{inc}(\boldsymbol{\rho}_n) = -\frac{E_0}{\eta_0} \frac{e^{-jkd_n}}{d_n} \ . \tag{4.10}$$

In both (4.9) and (4.10), d_n is given in (4.3). Using the radiation intensity integral in (4.5), the magnitude of the electric field can be related to the transmitted power as

$$E_0 = \sqrt{60 P_t} \ . \tag{4.11}$$

The isotropic radiator is located at 25 meters above $x = 0$. The receiver height is 2.4 meters. The total field results for both TM and TE polarizations are obtained via CBFM. Note that due to the big height variation, SA-FBM could not converge to a result. Hence, FBM is used as a reference solution. Total field results for $M = 50$, $M = 100$ and $M = 200$ are given in Fig. 4.9 (b), Fig. 4.9 (c), and Fig. 4.9 (d) for TM polarization, and Fig. 4.10 (b), Fig. 4.10 (c) and Fig. 4.10 (d) for TE polarization. In all cases, PBFs are obtained using physical optics and the blocks are extended by an amount of 1λ for the suppression of edge effects. For all cases (i.e., different M values), the non-uniform extrapolation is used in the following way for this terrain: Up to 3 kilometers, $l = 10$ is used uniformly. After 3 kilometers, l is increased to 50, because the surface profile is flatter. As a result, $\mathbf{u}_k^{(i)}$ is computed 15 times faster (i.e., $L_{eff} = 15$).

As can be observed from the plots in Fig. 4.9 and Fig. 4.10, CBFM results are in good agreement with the FBM results in all cases. Besides, one can see that results become more accurate as the number of blocks, M, is increased. This is expected since an increase in M leads to use of more CBFs which enables the current distribution to be represented more accurately. However, such an increase in the accuracy comes in the expense of increased CPU time because

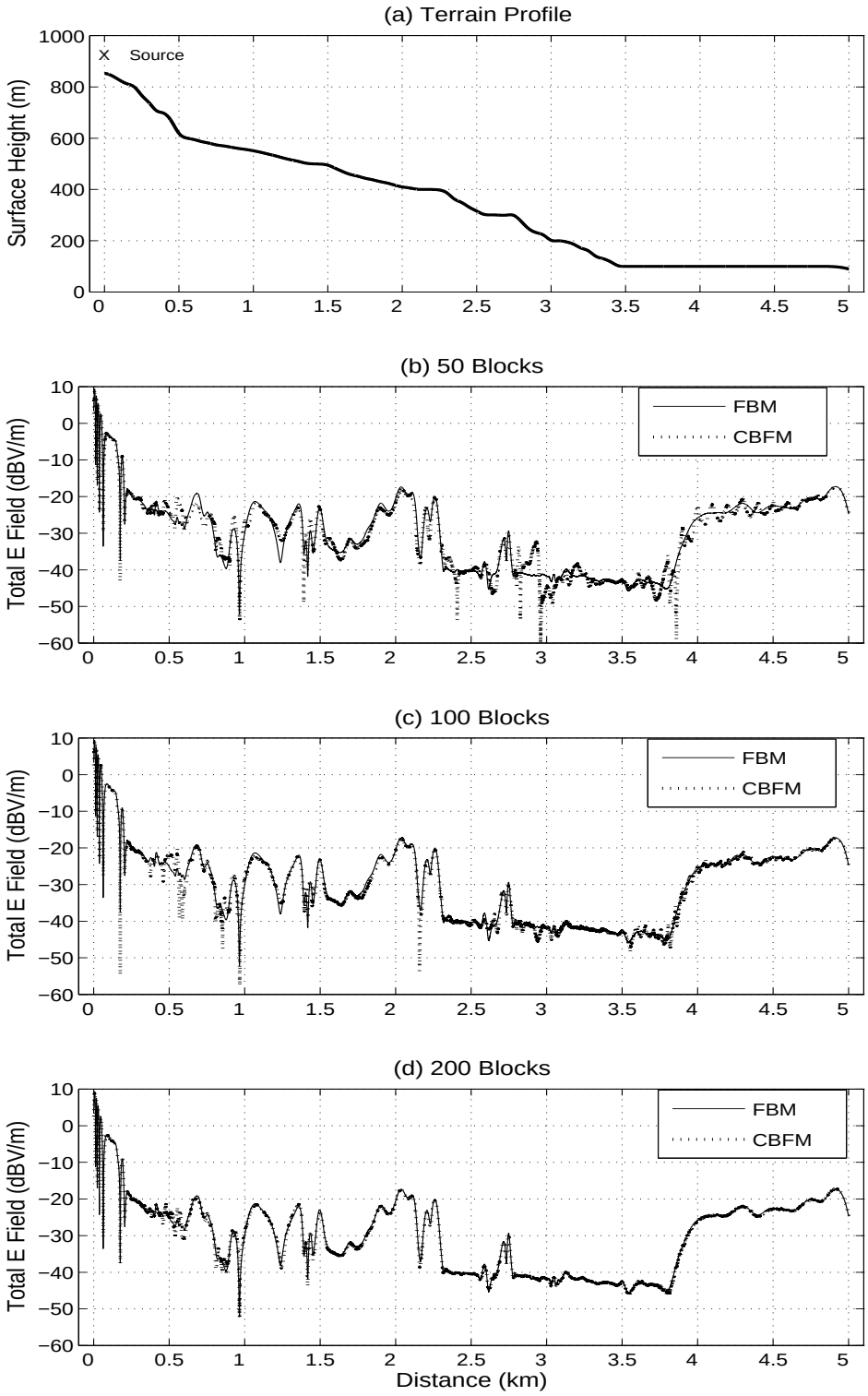

Figure 4.9: Total field for TM polarized isotropic radiator over a terrain profile from the west side of Turkey. Distance 5000 m, $N = 50000$, $L_{eff} = 15$.

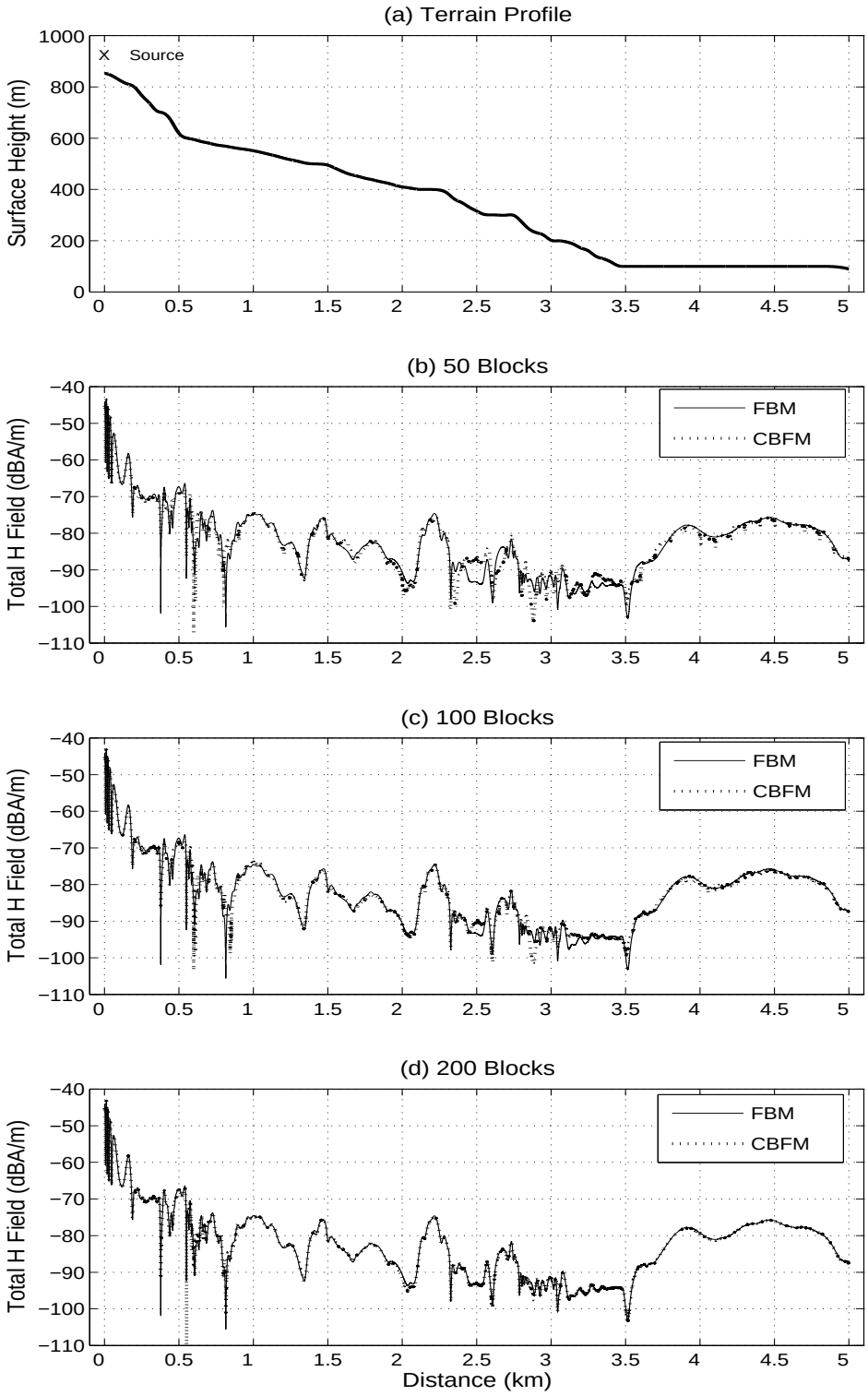

Figure 4.10: Total field for TE polarized isotropic radiator over a terrain profile from the west side of Turkey, Distance 5000 m, $N = 50000$, $L_{eff} = 15$.

	M	N_i	# of CBFs	# of iter.	CPU (s)/iter.	Total CPU (s)	Error (%)
fbm	-	-	-	6	7242	43452	-
cbfm	50	1000	148	-	-	1378	10.1
cbfm	100	500	298	-	-	2577	6.1
cbfm	200	250	598	-	-	8607	3.5

Table 4.1: Comparison of CPU times of CBFM with FBM and absolute errors for the terrain problem in Fig. 4.9 (a) for various M values (TM Pol.)

	M	N_i	# of CBFs	# of iter.	CPU (s)/iter.	Total CPU (s)	Error (%)
fbm	-	-	-	2	5794	11588	-
cbfm	50	1000	148	-	-	1308	10.8
cbfm	100	500	298	-	-	2543	8.2
cbfm	200	250	598	-	-	8590	3.4

Table 4.2: Comparison of CPU times of CBFM with FBM and absolute errors for the terrain problem in Fig. 4.10 (a) for various M values (TE Pol.)

of the additional inner products that are needed to be calculated during the generation of the reduced matrix. CPU times and absolute errors for various M values are given in Table 4.1 and Table 4.2 for TM and TE polarizations, respectively. Absolute percentage error of the CBFM is defined as

$$abs.\ error(\%) = \frac{||\mathbf{I}_{CBFM} - \mathbf{I}_{FBM}||_2}{||\mathbf{I}_{FBM}||_2} \times 100 \tag{4.12}$$

where $\mathbf{I}_{CBFM}$ and $\mathbf{I}_{FBM}$ are the CBFM and FBM currents, respectively and $||\ .\ ||_2$ indicates the Frobenious norm. In this example FBM is taken as a reference solution.

As depicted in Table 4.1 and Table 4.2, CBFM results are in good agreement with the FBM results but in a considerably less amount of time, even in the $M = 200$ case, where it takes approximately 8600 seconds for both TM and TE polarizations. This cost is comparable to a single iteration FBM result, which is about 7200 seconds for TM polarization and 5794 seconds for TE polarization. It should be noted that 6 iterations are required to obtain accurate FBM results for TM polarization whereas this number is only 2 for the TE case. Note that when $M = 50$, the required CPU times for CBFM are around 1400 seconds for both polarizations that are 5 times less than that of a single iteration FBM result for the TM case.

N		50000	50000	50000	N
M		200	100	50	M
L_{eff}		15	15	15	L_{eff}
Basis Functions	PBF	0.4	0.4	0.4	$O(N)$
	SBF	85	170	350	$O(N^2/M)$
	Total	85	171	350	$O(N^2/M)$
Reduced Matrix Gen.	$\mathbf{u}_k^{(i)}$	510	505	507	$O(N^2/L_{eff})$
	Inner Product	8012	1901	521	$O(N \times M^2)$
	Total	8522	2406	1028	
Total		8607	2577	1378	
FBM (1 iteration)		7242	7242	7242	$O(N^2)$

Table 4.3: CPU Times (s) for Different Stages of CBFM with Various Parameters

Table 4.3 presents the CPU times for different stages of CBFM for this example, in detail. One can realize that as the number of blocks, M, increases, reduced matrix generation part, more specifically, inner product operations of the CBFM procedure, dominates in terms of CPU times since its computational cost is $O(N \times M^2)$. On the other hand, with the use of the extrapolation process, CPU times for the generation of the $\mathbf{u}_k^{(i)}$ vectors, are substantially reduced. Note that further increase of L_{eff} does not bring an important reduction in CPU times. Although this part has $O(N^2/L_{eff})$ operational cost, L_{eff} parameter allows us to prevent rapid exponential growth in CPU times. Besides, it is obvious that CPU times for the generation of basis functions are negligible to some extent. Generation of PBFs does not depend on M since the use of PO is $O(N)$ operations. However, this is not valid for SBFs since we use FBM while generating SBFs. CPU times for SBFs and number of blocks, M, are inversely proportional. Hence, with a major decrease of M, generation of SBFs can be a dominant part of CBFM procedure. So it can be deduced that as long as M is kept in such a way that the generation of basis functions remains as the minor part in terms of CPU time, CBFM has $O(N)$ operational cost to some extent. Actually, this is illustrated in Fig. 4.11 for $M = 50$ and $M = 200$. Note that, as well as the generation of PBFs, inversion of the reduced matrix is also negligible since the matrix size is quite small.

In addition to number of blocks, M, we define a new parameter, nn, which represents the number of neighborhoods taken into account at each side of the

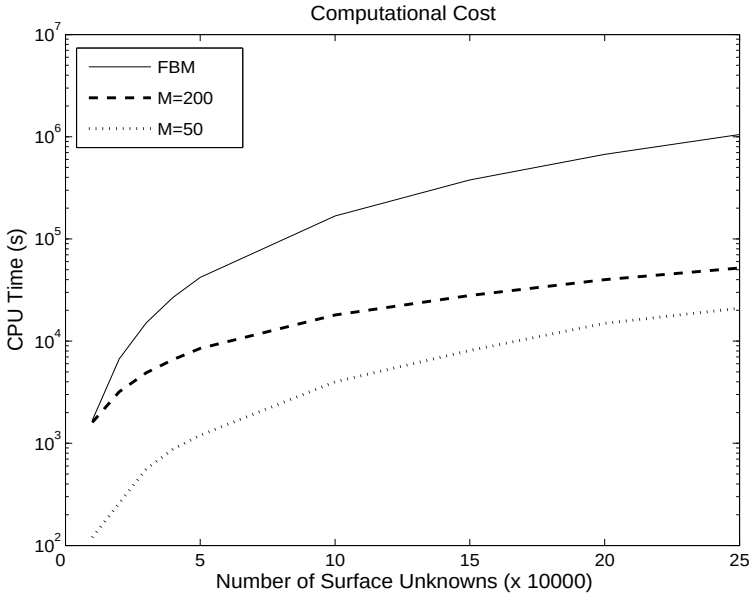

Figure 4.11: Comparison of CPU times with FBM for $M = 50$ and $M = 200$ with L_{eff}=15

extended block i, for the computation of SBFs. It should be noted that until now, we have implemented CBFM technique by taking only the adjacent blocks (i.e., $nn = 2$) for the generation of SBFs. For $nn = 4$, (3.6) should be modified as

$$\mathbf{V}_{N\times 1} = \sum_{k=1}^{3} \alpha_k^{(1)} \mathbf{u}_k^{(1)} + \sum_{k=1}^{4} \alpha_k^{(2)} \mathbf{u}_k^{(2)} + \sum_{k=1}^{5} \alpha_k^{(3)} \mathbf{u}_k^{(3)} + ...$$

$$+ \sum_{k=1}^{5} \alpha_k^{(M-2)} \mathbf{u}_k^{(M-2)} + \sum_{k=1}^{4} \alpha_k^{(M-1)} \mathbf{u}_k^{(M-1)} + \sum_{k=1}^{3} \alpha_k^{(M)} \mathbf{u}_k^{(M)} \tag{4.13}$$

which results in $5M - 6$ CBFs (M PBFs $+4M - 6$ SBFs).

For $nn = 6$, (3.6) should be modified as

$$\mathbf{V}_{N\times 1} = \sum_{k=1}^{4} \alpha_k^{(1)} \mathbf{u}_k^{(1)} + \sum_{k=1}^{5} \alpha_k^{(2)} \mathbf{u}_k^{(2)} + \sum_{k=1}^{6} \alpha_k^{(3)} \mathbf{u}_k^{(3)} + \sum_{k=1}^{7} \alpha_k^{(4)} \mathbf{u}_k^{(4)} + ...$$

$$+ \sum_{k=1}^{7} \alpha_k^{(M-3)} \mathbf{u}_k^{(M-3)} + \sum_{k=1}^{6} \alpha_k^{(M-2)} \mathbf{u}_k^{(M-2)} + \sum_{k=1}^{5} \alpha_k^{(M-1)} \mathbf{u}_k^{(M-1)} + \sum_{k=1}^{4} \alpha_k^{(M)} \mathbf{u}_k^{(M)} \tag{4.14}$$

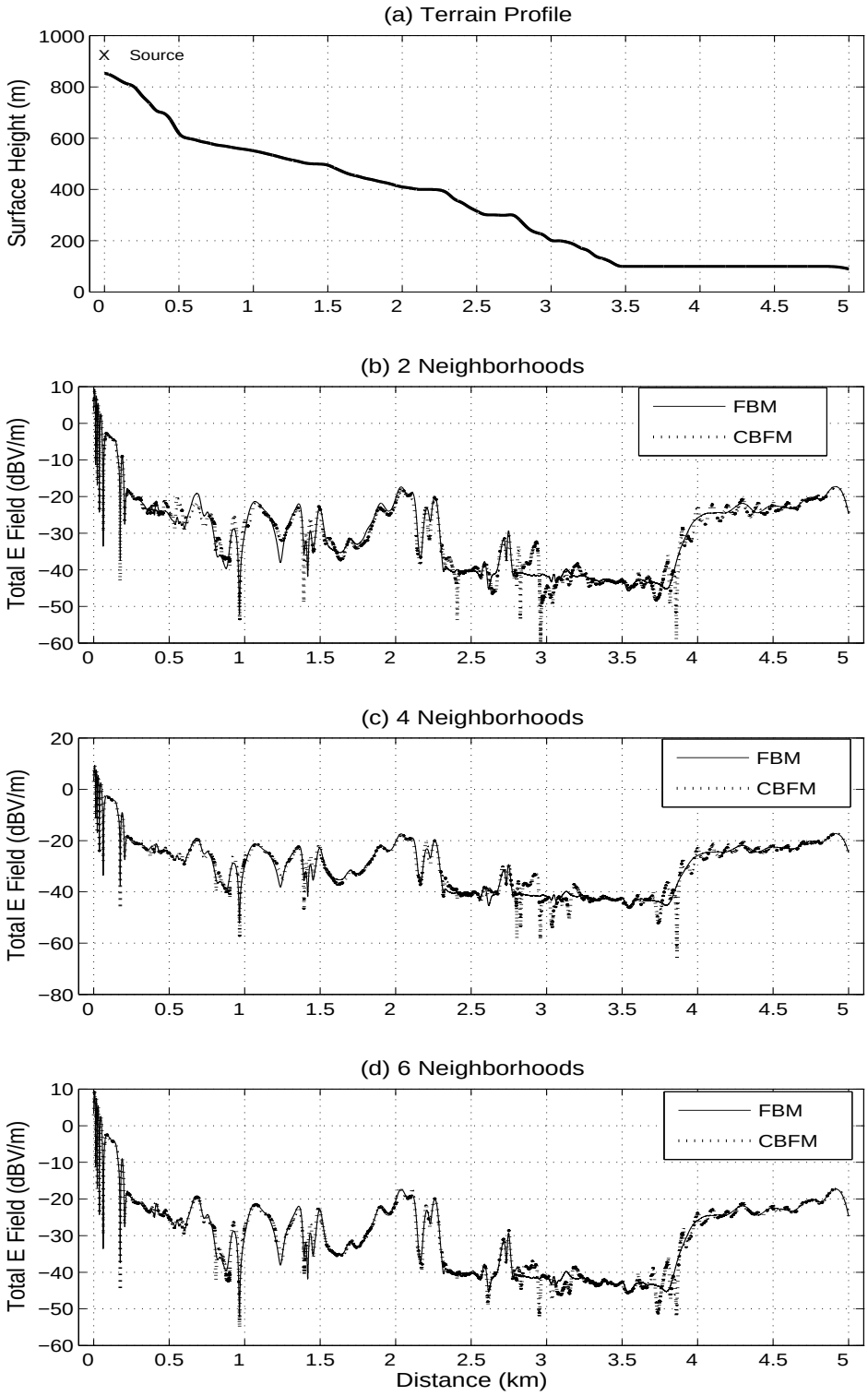

Figure 4.12: Total field for TM polarized isotropic radiator with various number of mutual interactions. Distance 5000 m, $N = 50000$, $M = 50$, $L_{eff} = 15$.

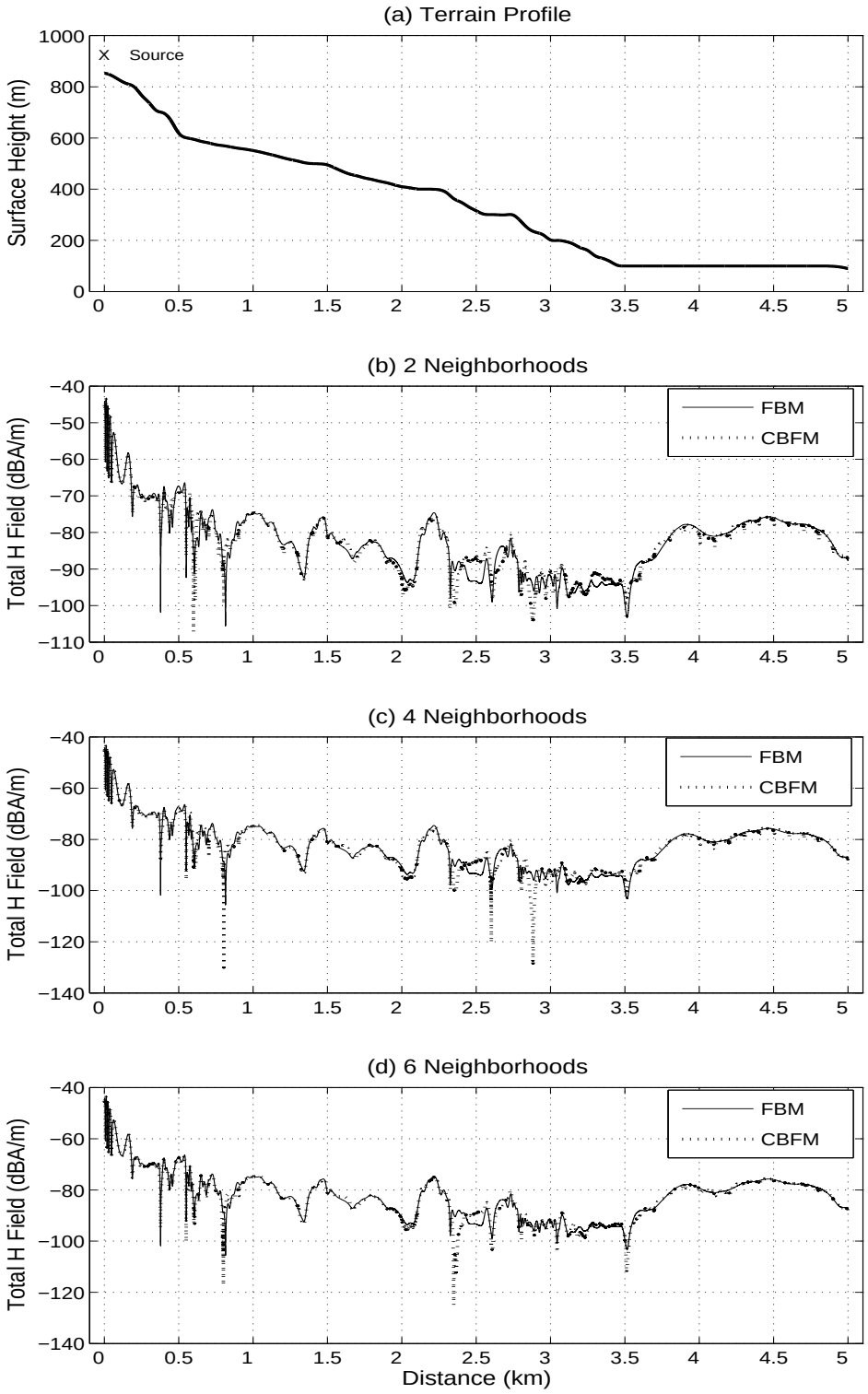

Figure 4.13: Total field for TE polarized isotropic radiator with various number of mutual interactions. Distance 5000 m, $N = 50000$, $M = 50$, $L_{eff} = 15$.

	N	M	nn	# of CBFs	Total CPU Time (s)	Error (%)
fbm	50000	-	-	-	43452	-
cbfm	50000	50	2	148 ($3M-2$)	1378	10.1
cbfm	50000	50	4	244 ($5M-6$)	2950	5.7
cbfm	50000	50	6	338 ($7M-12$)	5056	4.8
cbfm	50000	50	8	430 ($9M-20$)	7620	5.0

Table 4.4: Comparison of CPU times of CBFM with FBM and absolute errors for the terrain problem in Fig. 4.9 (a) for various nn values (TM Pol.)

N		50000	50000	50000	50000	N
nn		2	4	6	8	nn
Basis Functions	PBF	0.4	0.4	0.4	0.4	$O(N)$
	SBF	350	693	1028	1357	$O(N^2 \times nn/M)$
	Total	350	693	1028	1357	$O(N^2/M)$
Reduced Matrix Gen.	$\mathbf{u}_k^{(i)}$	507	836	1157	1478	$O(N^2 \times (nn+1)/L_{eff})$
	Inner Product	521	1450	2836	4721	$O(N \times M^2 \times (nn+1)^2)$
	Total	1028	2286	3993	6199	
Total		1378	2979	5021	7556	
FBM (1 iteration)		7242	7242	7242	7242	$O(N^2)$

Table 4.5: CPU Times (s) for Different Stages of CBFM with Various nn values. $M = 50$ and $L_{eff} = 15$

which results in $7M - 12$ CBFs (M PBFs + $6M - 12$ SBFs). With similar approach, for $nn = 8$, total number of CBFs turns out to be $9M - 20$.

Table 4.4 presents the CPU times and absolute errors for various nn values. Keep in mind that in an electrically large terrain, mutual interactions among far-away blocks are very weak. Thus, including more neighboring blocks does not improve the overall accuracy significantly in a uniform fashion. However, it is observed that when the field points are close to the source region, significant improvement is observed if two neighboring blocks on each side of the extended block i is included (i.e., $nn = 4$). This is an expected results because when the excitation is strong, mutual interactions among the blocks that are close to the excitation become also strong. Hence, inclusion of more mutual interactions naturally improves the accuracy in this region. Table 4.5 is the modified version of Table 4.3 with nn inserted as an explicit parameter into the formulation. Fig. 4.12 and Fig. 4.13 illustrates the total field distribution for varying nn values with $M = 50$ and $L_{eff} = 15$, for TM and TE polarizations.

Storage Requirements of CBFM

Previously, it was shown how CPU times vary with certain parameters such as the number of blocks, M, L_{eff} and nn. Likewise, memory storage of CBFM also changes with those parameters. CBFM is advantegeous in the sense that it does not require storage of any matrix except the reduced matrix as long as direct solvers for the generation of basis functions are not used which is the case for this study. Since basis functions are generated via the use of iterative solvers or physical optics, impedance matrices are not stored. However, basis functions and $\mathbf{u}_k^{(i)}$ vectors should be stored for the generation of the reduced matrix. Memory storage for the basis functions can be estimated as $(3M-2)\times N_i$ where $N_i = N/M$ and $(3M - 2) \times N/L_{eff}$ for $\mathbf{u}_k^{(i)}$ vectors. Thus, total memory storage turns out to be

$$storage \cong (3M - 2) \times \frac{N}{M} + (3M - 2) \times \frac{N}{L_{eff}} \tag{4.15}$$

for $nn = 2$. When more mutual interactions are taken into account (i.e., $nn \neq 2$), $(3M - 2)$ factor will be replaced by the corresponding values given in Table 4.4. Apparently, dominating part of the above sum is the storage of $\mathbf{u}_k^{(i)}$ vectors.

Fortunately, with the use of the extrapolation process, significant reduction can be obtained for the memory storage.

Chapter 5

Conclusions

In this study, an iteration-free, rigorous and efficient method, that combines CBFM, PO (when applicable) and FBM, is employed for the solution of IEs to investigate scattering from and propagation over large-scale rough terrain problems. The method is based on constructing macro-domain basis functions from the conventional sub-domain basis functions, with the help of PO and/or one iteration of FBM. It is further accelerated using a non-uniform extrapolation process throughout the terrain under investigation. CBFM has been applied for several terrain profiles with varying parameters in order to investigate its accuracy and to develop an efficient strategy for the solution of electromagnetic scattering from rough surfaces. In order to justify CBFM results, FBM and, if converges, SA-FBM are used as a reference solutions. CBFM results are also compared with measurement results obtained from real-world terrains.

CBFM is implemented for various kind of excitations such as isotropic radiator, dipole antenna and plane wave. It has been shown that performance of CBFM is independent of the excitation due to its iteration-free nature.

Implementation of CBFM involves determination of some parameters. Since they turn out to make a considerable effect on CPU times and memory usage, critical parameters are number of blocks while partitioning the surface profile and number of mutual interactions taken into account while generating SBFs. It has

been observed that selecting number of blocks around 50 and 100 for problems with unknowns at the order of 20000-300000 results in a good optimization between accuracy and computational cost. Further increase causes more usage of memory and more CPU times since it brings additional inner product operations for construction of the reduced matrix, whereas further decrease of number of blocks also brings additional CPU times since, this time, basis function generations start to dominate due to its $O(N^2/M)$ operational cost.

On the other hand, numerical results show that it yields very accurate results to take only the mutual interactions of neighboring blocks into account while generating SBFs. This is due to the fact that in an electrically large profile, mutual interactions among far-away blocks are very weak. However, it is observed that when the field points are close to source region, significant improvement is observed if more neighboring blocks on each side of a block are included (i.e., $nn \neq 2$). This is an expected result because when the excitation is strong, mutual interactions among the blocks that are close to the excitation become also strong. Hence, inclusion of more mutual interactions naturally improves the accuracy in this region. However, increase in the CPU times and the storage requirements is again an issue.

One of the future works is to apply CBFM to re-entrant surface profiles. Although GFBM and its spectral accelerated version GFBSA have been proposed, these approaches cannot reduce the $O(N^3)$ operational count arising in the direct inversion of the obstacle region self-interaction matrix.

Appendix A

Spectral Acceleration for the Backward Propagation

A.1 Horizontal Polarization

Starting with the formulation of the EFIE described in Section 2.1 for the horizontal polarization, the radiated electric field at $\boldsymbol{\rho}_n$ due to the forward propagation E_f and backward propagation E_b can be obtained as:

$$E_f(\boldsymbol{\rho}_n) = \sum_{m=1}^{n-1} I_m Z_{nm} \tag{A.1}$$

$$E_b(\boldsymbol{\rho}_n) = \sum_{m=n+1}^{N} I_m Z_{nm}. \tag{A.2}$$

E_b is decomposed into the fields radiated by the strong and weak groups, E_s and E_w respectively,

$$\begin{aligned} E_b(\boldsymbol{\rho}_n) &= E_s(\boldsymbol{\rho}_n) + E_w(\boldsymbol{\rho}_n) \\ &= \sum_{m=n+N_s}^{n+1} I_m Z_{nm} + \sum_{m=N}^{n+N_s+1} I_m Z_{nm} \end{aligned} \tag{A.3}$$

where $N_s = L_s/\Delta x$ denotes the number of elements that have strong interactions with the nth element. The off-diagonal entries of the impedance matrix for the

horizontal polarization were derived using the EFIE in Section 2.1 for non-PEC surfaces as

$$Z_{nm} = -j\omega\mu G(\boldsymbol{\rho}_n, \boldsymbol{\rho}_m)\Delta x_m + \eta_m \Delta x_m \frac{\partial}{\partial n_m} G(\boldsymbol{\rho}_n, \boldsymbol{\rho}_m). \tag{A.4}$$

The radiation of the strong interaction group is computed directly through a matrix-vector product, but the weak group contribution is obtained by employing the spectral representation of the Green's function and its derivative. The spectral representation of the Green's functions can be expressed as

$$G(\boldsymbol{\rho}_n, \boldsymbol{\rho}_m) = -\frac{j}{4\pi} \int_{C_\phi} e^{-jk[(x_n - x_m)\cos\phi + (z_n - z_m)\sin\phi]} d\phi \tag{A.5}$$

where C_ϕ is the contour of integration in the complex ϕ-space (shown in Fig. 2.5). On the other hand, the spectral representation of the partial derivative of the Green's function with respect to the normal vector on source point can be expressed as:

$$\frac{\partial}{\partial n_m} G(\boldsymbol{\rho}_n, \boldsymbol{\rho}_m) = \frac{k}{4\pi} \int_{C_\phi} [\cos\theta_m \cos\phi + \sin\theta_m \sin\phi] e^{-jk[(x_n - x_m)\cos\phi + (z_n - z_m)\sin\phi} d\phi \tag{A.6}$$

where θ_m is the angle between the unit normal vector to the surface at the source point, $\hat{n}_m$, and the unit vector in the $-x$ direction, -$\hat{x}$. Substituting (A.5) and (A.6) into the expression for $E_w(\boldsymbol{\rho}_n)$ and interchanging the integration and summation yields to:

$$E_w(\boldsymbol{\rho}_n) = -\frac{\omega\mu}{4\pi} \int_{C_\phi} F_n(\phi) d\phi \tag{A.7}$$

where

$$F_n(\phi) = \sum_{m \in G_w} I_m \Delta x_m \left(1 - \frac{\eta_m}{\eta_0}[\cos\theta_m \cos\phi + \sin\theta_m \sin\phi]\right) \cdot e^{-jk[(x_n - x_m)\cos\phi - (z_n - z_m)\sin\phi]}. \tag{A.8}$$

$F_n(\phi)$ can be obtained from $F_{n+1}(\phi)$ as:

$$\begin{aligned} F_n(\phi) &= F_{n+1}(\phi) e^{-jk[(x_n - x_{n+1})\cos\phi - (z_n - z_{n+1})\sin\phi]} \\ &+ I_{ns} \Delta x_{ns} \left(1 - \frac{\eta_{ns}}{\eta_0}[\cos\theta_{ns}\cos\phi + \sin\theta_{ns}\sin\phi]\right) \\ &\cdot e^{-jk[(x_n - x_{ns})\cos\phi - (z_n - z_{ns})\sin\phi]} \end{aligned} \tag{A.9}$$

with $F_n(\phi) = 0$ for $n \geq N - N_s$, and $n_s = n + N_s + 1$ is the new source point introduced in the weak group as the iterative procedure sweeps the surface in the backward direction.

A.2 Vertical Polarization

In a similar way, when using the MFIE formulation in the vertical polarization case, the radiating elements are also divided into 2 groups (G_s and G_w) and their contribution to the forward magnetic field H_f can be expressed as follows

$$H_b(\boldsymbol{\rho}_n) = H_s(\boldsymbol{\rho}_n) + H_w(\boldsymbol{\rho}_n)$$

$$= \sum_{m=n+N_s}^{n+1} I_m Z_{nm} + \sum_{m=N}^{n+N_s+1} I_m Z_{nm} \tag{A.10}$$

where H_w and H_s are the fields radiated by the weak and strong groups, respectively, and Z_{nm} is defined in Section 2.1 as

$$Z_{nm} = j\omega\epsilon\eta_m \Delta x_m G(\boldsymbol{\rho}_n, \boldsymbol{\rho}_m) - \Delta x_m \frac{\partial}{\partial n_m} G(\boldsymbol{\rho}_n, \boldsymbol{\rho}_m). \tag{A.11}$$

Using the spectral representation of Green's function and its derivative, contribution due to the weak group can be expressed as:

$$H_w(\boldsymbol{\rho}_n) = -\frac{k}{4\pi} \int_{C_\phi} F_n(\phi) d\phi \tag{A.12}$$

where

$$F_n(\phi) = \sum_{m \in G_w} I_m \Delta x_m \left(\cos\theta_m \cos\phi + \sin\theta_m \sin\phi - \frac{\eta_m}{\eta_0} \right)$$

$$\cdot e^{-jk[(x_n - x_m)\cos\phi - (z_n - z_m)\sin\phi]}. \tag{A.13}$$

Then $F_n(\phi)$ can be obtained from $F_{n+1}(\phi)$ like in (A.9) except the term inside the paranthesis is changed with $\left(\cos\theta_{ns}\cos\phi + \sin\theta_{ns}\sin\phi - \frac{\eta_{ns}}{\eta_0}\right)$.

Bibliography

[1] L. Tsang, J. A. Kong, and K. -H. Ding *Scattering of Electromagnetic Waves: Theories and Applications*, New York: Wiley, 2000.

[2] L. Tsang, J. A. Kong, K. -H. Ding, and C. A. Ao *Scattering of Electromagnetic Waves: Numerical Solutions*, NJ: Wiley, 2001.

[3] R. F. Harrington, *Field Computation by Moment Method*, New York: IEEE Press, 1993.

[4] J. C. West and J. M. Sturm, "On iterative approaches for electromagnetic rough-surface scattering problems," *IEEE Trans. Antennas and Propagat.*, Vol. 47, no. 8, pp. 1281-1288, Aug. 1999.

[5] C. F. Smith, A. F. Peterson, and R. Mittra "The biconjugate gradient method for electromagnetic scattering," *IEEE Trans. Antennas and Propagat.*, Vol. 38, no. 6, pp. 938-940, June 1990.

[6] F. Chen "The numerical calculation of two-dimensional rough surface scattering by the conjugate gradient method," *Int. J. Remote Sens.*,Vol. 17, no. 4, pp. 801-808, 1996.

[7] D. Holliday, L. L. DeRaad Jr., and G. J. St.-Cyr, "Volterra approximation for low grazing angle shadowing ocean-like surfaces," *IEEE Trans. Antennas and Propagat.*, Vol. 43, no. 11, pp. 1199-1206, Nov. 1996.

[8] D. Holliday, L. L. DeRaad Jr., and G. J. St.-Cyr, "Forward-Backward: A new method for computing low-grazing angle scattering," *IEEE Trans. Antennas and Propagat.*, Vol. 44, no. 5, pp. 722-729, May 1996.

[9] D. A. Kapp and G. S. Brown, "A new numerical method for rough surface scattering calculations," *IEEE Trans. Antennas and Propagat.*, Vol. 44, no. 5, pp. 711-721, May 1996.

[10] D. Holliday, L. L. DeRaad Jr., and G. J. St.-Cyr, "Forward-Backward method for scattering from imperfect conductors," *IEEE Trans. Antennas and Propagat.*, Vol. 46, pp. 101-107, Jan. 1998.

[11] H. -T. Chou, J. T. Johnson, "A novel acceleration algorithm for the computation of scattering from rough surfaces with the forward-backward method," *Radio Sci.*, Vol. 33, no. 5, pp. 1277-1287, Sep. /Oct. 1998.

[12] H. -T. Chou, J. T. Johnson, "Formulation of forward-backward method using novel spectral acceleration for the modeling of scattering from impedance rough surface," *IEEE Trans. Geosci. Remote Sens.*, Vol. 38, pp. 605-607, Jan. 2000.

[13] J. A. López, M. R. Pino, F. Obelleiro, J. L. Rodríguez, "Application of the spectral acceleration forward-backward method to coverage analysis over terrain profiles," *J. of Electromagn. Waves and Appl.*, Vol. 15, pp. 1049-1074, Aug. 2001.

[14] V. V. S. Prakash, Raj Mittra, "Characteristic basis function method: A new technique for efficient solution of method of moments matrix equations," *Microwave and Optical Technology Letters*, Vol. 36, No. 2, pp. 95-100, Jan. 2003.

[15] G. Tiberi, S. Rosace, A. Monorchio, G. Manara and R. Mittra, "Electromagnetic scattering from large faceted conducting bodies by using analytically derived characteristic basis functions," *Antennas and Wireless Propagation Letters, IEEE*, Vol. 2, pp. 290-293, 2003.

[16] R. Mittra, J.-F. Ma, E. Lucente, and A. Monorchio, "CBMOM - an iteration free MoM approach for solving large multiscale EM radiation and scattering problems," *Antennas and Propagation Society International Symposium, 2005 IEEE*, Vol. 2B, pp. 2-5, July 2005.

[17] S. J. Kwon, K. Du, Raj Mittra, "Characteristic basis function method: A numerically efficient technique for analyzing microwave and rf circuits," *Microwave and Optical Technology Letters*, Vol. 38, No. 6, pp. 444-448, Sept. 2003.

[18] J. Yeo, V. V. Prakash, Raj Mittra, "Efficient analysis of a class of microstrip antennas using the characteristic basis function method (CBFM)," *Microwave and Optical Technology Letters*, Vol. 39, No. 6, pp. 456-464, Dec. 2003.

[19] G. Tiberi, A. Monorchio, G. Manara and R. Mittra, "A spectral domain integral equation method utilizing analytically derived characteristic basis functions for the scattering from large faceted objects," *Antennas and Wireless Propagation Letters, IEEE*, Vol. 54, pp. 2508-2514, Sept. 2006.

[20] E. Lucente, A. Monorchio, and R. Mittra, "Generation of characteristic basis functions by using sparse MoM impedance matrix to construct the solution of large scattering and radiation problems," *Antennas and Propagation Society International Symposium, 2006, IEEE*, pp. 4091-4094, 2006.

[21] E. Lucente, A. Monorchio, and R. Mittra, "An iteration-free MoM approach based on excitation independent characteristic basis functions for solving large multiscale electromagnetic scattering problems," *IEEE Trans. Antennas and Propagat.*, vol. 56, no. 4, pp. 999-1007, April 2008.

[22] E. Garcia, C. Delgado, I. G. Diego, and M. F. Catédra, "An iterative solution for electrically large problems combining the characteristic basis function method and the multilevel fast multipole algorithm," *IEEE Trans. Antennas and Propagat.*, vol. 56, no. 8, pp. 2363-2371, August 2008.

[23] A. Yagbasan, C. A. Tunc, V. B. Ertürk, A. Altintas and R. Mittra, "Application of characteristic basis function method for scattering from and propagation over terrain problems," *EMTS 2007-International URSI Commission B-Electromagnetics Theory Symposium*, Ottawa, Canada, July 26-28, 2007.

[24] A. Yagbasan, C. A. Tunc, V. B. Ertürk, A. Altintas and R. Mittra, "Use of characteristic basis function method for scattering from terrain profiles," *Turk. J. Elec. Eng. & Comp. Sci.*, vol. 16, no. 1, pp. 33-39, 2008.

[25] T. B. A. Senior, "Impedance boundary conditions for imperfectly conducting surfaces," *Applied Scientific Research*, Vol. 8, pp. 418-436, 1961.

[26] D. -S. Wang, "Limits and validity of the impedance boundary condition on penetrable surfaces," *IEEE Trans. Antennas Propagat.*, Vol. AP-35, pp. 453-457, Apr. 1987.

[27] S. -W. Lee and W. Gee, "How good is the impedance boundary condition?", *IEEE Trans. Antennas Propagat.*, Vol. 50, pp. 1313-1315, Nov. 1987.

[28] C. A. Balanis, "*Advanced Engineering Electromagnetics*," John Wiley & Sons, 1989.

[29] J. M. Sturm, J. C. West, "Numerical study of shadowing in electromagnetic scattering from rough dielectric surfaces", *IEEE Trans. Geosci. Remote Sens.*, Vol. 36, pp. 1477-1484, Sept. 1998.

[30] C. A. Tunç, "Application of spectral acceleration forward-backward method for propagation over terrain," *M.S. Thesis in Electrical and Electronics Engineering*, Bilkent University, Sept. 2003.

[31] M. R. Pino, L. Landesa, J. L. Rodríguez and F. Obelleiro, "The generalized forward-backward method for analyzing the scattering for targets on ocean-like rough surfaces," *IEEE Trans. Antennas and Propagat.*, Vol. 47, pp. 961-969, June 1999.

[32] M. R. Pino, R. J. Burkholder, and F. Obelleiro, "Spectral acceleration of the generalized forward-backward method," *IEEE Trans. Antennas and Propagat.*, Vol. 50, pp. 785-797, June 2002.

[33] C. A. Tunc, V. B. Ertürk, A. Altintas, "Examination of existent propagation models over large inhomogeneous terrain profiles using fast integral equation solution," *IEEE Trans. Antennas Propagat.*, Vol. 53, no. 9, pp. 3080-3083, September 2005.

[34] J. Shaeffer, "Direct solve of electrically large integral equations for problem sizes to 1 m unknowns," *IEEE Trans. Antennas and Propagat.*, vol. 56, no. 8, pp. 2306-2313, August 2008.

[35] C. A. Balanis, "*Antenna Theory: Analysis and Design*," John Wiley & Sons, 1982.

[36] J. Hviid, J. Andersen, J. Toftgard, and J. Bojer, "Terrain-based propagation model for rural area-an integral equation approach," *IEEE Trans. Antennas and Propagat.*, vol. 43, no. 1, pp. 41-46, Jan. 1995.